NEUROSCIENCE

Recapitulating and reversing human brain ribosomopathy defects via the maladaptive integrated stress response

Wei Zhang[1], Minjie Zhang[2], Li Ma[1], Supawadee Jariyasakulroj[1], Qing Chang[1], Ziying Lin[1], Zhipeng Lu[2], Jian-Fu Chen[1]*

Animal or human models recapitulating brain ribosomopathies are incomplete, hampering development of urgently needed therapies. Here, we generated genetic mouse and human cerebral organoid models of brain ribosomopathies, caused by mutations in small nucleolar RNA (snoRNA) *SNORD118*. Both models exhibited protein synthesis loss, proteotoxic stress, and p53 activation and led to decreased proliferation and increased death of neural progenitor cells (NPCs), resulting in brain growth retardation, recapitulating features in human patients. Loss of *SNORD118* function resulted in an aberrant upregulation of p-eIF2α, the mediator of integrated stress response (ISR). Using human iPSC cell–based screen, we identified small-molecule 2BAct, an ISR inhibitor, which potently reverses mutant NPC defects. Targeting ISR by 2BAct mitigated ribosomopathy defects in both cerebral organoid and mouse models. Thus, our *SNORD118* mutant organoid and mice recapitulate human brain ribosomopathies and cross-validate maladaptive ISR as a key disease-driving mechanism, pointing to a therapeutic intervention strategy.

INTRODUCTION

Ribosomopathies are a group of human disorders caused by mutations in ribosomal proteins (RPs) or ribosome biogenesis factors (*1*, *2*). Protein synthesis loss, proteotoxicity gain, and p53 activation are hallmark cellular defects in ribosomopathies (*3*–*5*). Ribosome biogenesis disruption is expected to cause a reduction of functional ribosome units coupled with protein synthesis loss, resulting in global and mRNA-specific translation dysregulation (*2*, *3*). Meanwhile, ribosome acts as an integrated machine containing hundreds of RPs and ribosomal RNAs (rRNAs). Loss of one ribosome biogenesis factor generates a large number of orphan RPs and rRNAs (*4*, *6*), which overload the cellular degradation systems, leading to the proteotoxic stress. Our understanding of protein synthesis loss and proteotoxicity gain in ribosomopathies remains incomplete, which hampers the development of mechanism-based targeting strategies.

Ribosome biogenesis is a fundamental housekeeping process, which is universally required for mRNA translation and protein synthesis in all cells (*2*, *7*). Individual ribosomopathies preferentially affect specific tissue types, such as bone marrow–derived cells and skeletal tissues. Brain development requires highly sophisticated regulations in cell fate, neural progenitor cell (NPC) proliferation and differentiation, neuronal morphology, and synaptogenesis (*8*, *9*). Adding another layer of complexity is that human brain undergoes an evolutionary expansion in development due to the primate-enriched outer subventricular zone (oSVZ) (*10*). Human induced pluripotent stem cells (hiPSCs) and hiPSC-derived brain organoids provide a platform for experimentally addressing early human neurodevelopmental processes associated with neuropsychiatric disorders in a relevant genetic and cellular context (*10*–*12*). The rapid proliferation and growth of NPCs in early development generate a temporarily high level of demand for transcriptional output and protein synthesis (*13*, *14*). Temporal changes in protein synthesis have been observed in the developing cerebral cortex (*14*–*16*). Despite the progress made thus far, our understanding of the regulation and function of ribosome biogenesis in the brain, particularly in the context of human brains, remains limited.

The integrated stress response (ISR) is activated by a wide range of pathophysiological stress conditions, leading to the inhibition of global protein synthesis. The converging point for diverse stress stimuli that activate ISR is the phosphorylation of the α subunit of eukaryotic translation initiation factor 2 (eIF2α) on serine-51 (*17*, *18*). This phosphorylation converts eIF2 from a substrate to its competitive inhibitor of eIF2B, the key regulator of protein synthesis initiation. Recently, it has been reported that ribosomopathy-associated mutations trigger proteotoxic stress, which is marked by the up-regulation of eIF2α. Meanwhile, this eIF2α up-regulation acts as the mediator of ISR, which is proposed to provide cytoprotective roles because it contributes to the limitation of the proteotoxic stress caused by RP deficiency (*4*). However, severe stress due to its increased intensity or duration can convert ISR's cytoprotective roles to pathologically maladaptive functions, which have not been investigated in ribosomopathies. Overall, the long-term roles of ISR and their implications for therapeutic interventions in ribosomopathies remain largely unknown.

SNORD118 belongs to the family of small nucleolar RNAs (snoRNAs), a class of small RNA molecules that guide chemical modifications of rRNAs (*19*–*21*). *SNORD118* encodes the box C/D snoRNA U8 that is required for rRNA maturation (*22*, *23*). U8 loss impairs the cleavage of pre-rRNA and rRNA processing and modification leading to ribosome biogenesis defects (*24*, *25*). *SNORD118* mutations in humans cause ribosomopathies with purely neurological manifestations, including severe developmental delay and defects in cerebral white matter, which can impair cognitive and motor functions (*26*, *27*). These disease-associated changes are generally recessive loss-of-function compound heterozygous or homozygous mutations (*27*). Here, we have generated the first genetic mouse and

[1]Center for Craniofacial Molecular Biology, University of Southern California, Los Angeles, CA 90033, USA. [2]Department of Pharmacology and Pharmaceutical Sciences, University of Southern California, Los Angeles, CA 90089, USA.
*Corresponding author. Email: jianfu@usc.edu

human cerebral organoid models of *SNORD118* ribosomopathies. *SNORD118* mutations caused protein synthesis loss and proteotoxic stress leading to NPC fate and brain developmental defects. These defects were mechanistically linked with the maladaptive ISR activation in brain. Significantly, pharmacological targeting this maladaptive brake of protein synthesis by small-molecule 2BAct can mitigate all evaluated brain ribosomopathy-like defects in cerebral organoid and mouse models. Therefore, our genetic mouse and organoid models cross-validate maladaptive ISR as the key disease driving mechanism of ribosomopathies, pointing to a therapeutic intervention strategy.

RESULTS

Cerebral organoid models reveal reduced neurons and organoid sizes due to *SNORD118* mutations

SNORD118 mutations cause severe developmental delay including brain growth retardation (*26*, *27*). To establish human cerebral organoid models, we generated *SNORD118*-mutant hiPSCs using CRISPR-Cas9 approach. While homozygous knockout (KO) of hiPSC lines cannot be obtained due to early lethality, we produced three independent heterozygous mutants hiPSC lines that carry 16– or 6–base pair deletion (fig. S1A). *SNORD118* encodes U8 snoRNA, and quantitative polymerase chain reaction (qPCR) results showed that the expression level of U8 was reduced in mutant cell lines (fig. S1B), which mimics U8 down-regulation in patients (*26*, *27*). To model human brain development, we generated and characterized *SNORD118*$^{+/-}$ heterozygous cerebral organoids with isogeneic controls. At weeks 4 and 6, there were no differences between control and *SNORD118*$^{+/-}$ cerebral organoids, while at week 8, *SNORD118*$^{+/-}$ cerebral organoids showed a smaller size and significantly reduced surface areas compared to controls (Fig. 1, A and B). To investigate the cellular basis of reduced organoid sizes, we performed immunohistochemical (IHC) staining and examined T-Brain-1 (TBR1)–labeled layer V-VI neurons and Special AT-rich sequence-binding protein 2 (SATB2)–labeled layer II-V neurons (*28*). There is a significant decrease in TBR1- and SATB2-positive neurons in the ventricular zone (VZ)/SVZ–like regions of *SNORD118*$^{+/-}$ organoids compared to controls (Fig. 1, C to F). These results suggest that *SNORD118* is required for neuron production during human brain development. To investigate how *SNORD118* disease mutations affect human brain development, we focused on homozygous *5C>G point mutations, which occur repeatedly in patient families (*26*, *27*). We combined single-stranded oligodeoxynucleotides (ssODNs) with CRISPR-Cas9 complex to introduce disease-specific mutation into hiPSCs and generated homozygous *SNORD118*$^{*5C>G}$ point mutations, which contain C to G changes in the 3′ extension region of *SNORD118*. The DNA sequence of three independent lines confirmed *SNORD118*$^{*5C>G}$ homozygous mutations. We then generated *SNORD118*$^{*5C>G}$ homozygous mutant cerebral organoids with isogeneic controls. Whereas no difference was detected in week 4 organoids, *SNORD118*$^{*5C>G}$ mutant cerebral organoids showed a smaller size at 6- to 8-week-old ages with significantly reduced surface areas (Fig. 1, G and H). IHC staining showed that TBR1-positive layer V-VI and SATB2-positive layer II-V neurons were significantly decreased in the *SNORD118*$^{*5C>G}$ homozygous mutant cerebral organoids (Fig. 1, I to L). Together, we established cerebral organoid models of *SNORD118* mutations and revealed a decrease in neuron production, which mimics patient brain growth retardation symptoms.

Ribosomopthy hallmark cellular defects lead to reduced NPCs in *SNORD118*-mutant cerebral organoids

Brain growth retardation could be caused by the disruption of NPCs and is modeled by cerebral organoids (*11*, *29*). To investigate the causes of reduced neurons and organoid sizes, we focused on NPCs with *SNORD118*$^{*5C>G}$ homozygous mutations, which are more disease relevant compared to heterozygous mutations. Paired box protein Pax-6 (PAX6) and TBR2 were used to label apical neural progenitor cells (APCs) and intermediate neural progenitor cells (IPCs), respectively. There is a significant decrease in the percentage of PAX6-positive APCs and TBR2-positive IPCs in the VZ/SVZ-like regions of *SNORD118*$^{*5C>G}$ mutant cerebral organoids compared to isogenic controls (Fig. 2, A to D). Therefore, there is a significant reduction of NPC numbers in mutant cerebral organoids compared to controls.

Cell cycle progression is frequently disrupted in affected tissues in ribosomopathies (*2*). To study the causes of reduced NPCs in mutant organoids, we used phospho-Histon 3 (p-H3) to label mitotic cells and found that *SNORD118*$^{*5C>G}$ mutations cause reduced p-H3–postive NPCs, which are marked by SRY-Box Transcription Factor 2 (SOX2) (Fig. 2, E and F). Bromodeoxyuridine (BrdU) incorporation assay and Ki67 staining showed that there is a significant decrease in the percentage of BrdU- and Ki67-positive cells in mutant cerebral organoids (Fig. 2, G and H). Therefore, NPCs in *SNORD118*$^{*5C>G}$ cerebral organoids exhibited a reduction in cell proliferation, which is a typical cellular defect commonly found in vulnerable cell types in ribosomopathies. *SNORD118* mutation-mediated proliferation reduction also explains the reduced numbers of NPCs and neurons leading to smaller cerebral organoid sizes. Ribosomopathy studies across different tissues and disease models showed that ribosome biogenesis disruption activates p53 signaling, which, in turn, causes cell cycle arrest and apoptosis. Therefore, we examined p53 and found a significant increase in the percentage of p53-positive cells in the VZ/SVZ-like regions of mutant cerebral organoids (Fig. 2, I and J). Cleaved Caspase 3 is used for detecting early stages of apoptosis. To examine the consequence of sustained p53 activation, we performed IHC staining of Caspase 3 and found a significant increase in Caspase 3–positive cells in the mutant cerebral organoids compared to controls (Fig. 2, K and L).

The activation of p53 is expected to increase levels of cell cycle inhibitor p21, which binds to and inhibits cyclin-dependent kinases (CDKs). By inhibiting CDKs, p21 prevents the phosphorylation of proteins involved in the cell cycle, leading to a cell cycle arrest at G_1-S or G_2-M checkpoint (*30*). Therefore, we focused on p21 as the cell cycle arrest marker and found a significant increase in the percentage of p21-positive NPCs labeled by SOX2 within the VZ/SVZ-like regions of mutant cerebral organoids (Fig. 2, M and N). To investigate which cell cycle phase has been arrested, we turned to our human iPSC-derived NPCs in vitro. We synchronized NPCs using nocodazole treatment (*31*), followed by nocodazole withdrawal to allow them to restart the cell cycle (fig. S1C). There was a reduction in Ki67-, Ethynyl deoxyuridine (EdU)–, and p-H3–positive cells and an increase in p21-positive cells in mutant iPSC-derived NPCs (fig. S1, D and E). To identify the arrested phase, we conducted propidium iodide staining based on the distinct DNA content associated with each cell cycle phase. There were no significant differences in the percentage of G_0-G_1 phase cells between control and mutant NPCs. Whereas S phase population was reduced in mutant NPCs, the G_2-M phase cells were increased in mutants compared to

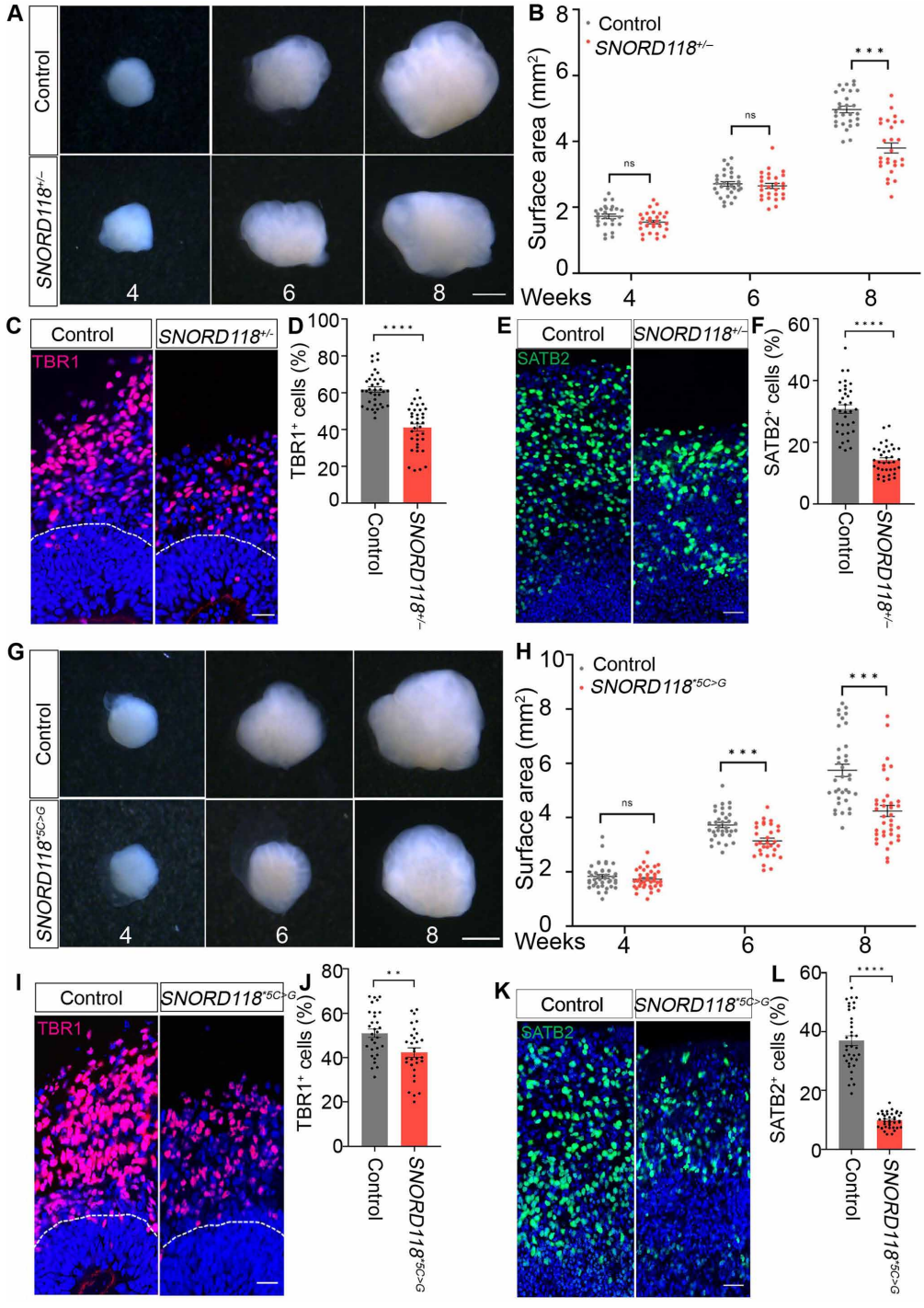

Fig. 1. Cerebral organoid models reveal reduced neurons and organoid sizes with *SNORD118* mutations. (**A**) Bright-field images of control and *SNORD118*$^{+/-}$ cerebral organoids at 4, 6, and 8 weeks. Scale bar, 1 mm. (**B**) Quantification of surface areas of control and *SNORD118*$^{+/-}$ cerebral organoids. $N = 26$ to 30 organoids from three independent lines. (**C** and **E**) Immunofluorescent staining for TBR1 (red) or SATB2 (green) in control and *SNORD118*$^{+/-}$ cerebral organoids. Scale bars, 50 μm. (**D** and **F**) Quantification of TBR1- or SATB2-labeled neurons in cerebral organoids. $N = 36$ cortex-like structures from 12 organoids of three independent lines. (**G**) Bright-field images of control and *SNORD118*$^{*5C>G}$ homozygous mutant cerebral organoids at 4, 6, and 8 weeks. Scale bar, 1 mm. (**H**) Quantification of surface areas of control and *SNORD118*$^{*5C>G}$ homozygous mutant cerebral organoids. $N = 31$ to 39 organoids from three independent lines. (**I** and **K**) Immunofluorescent staining for TBR1 (red) and SATB2 (green) in cerebral organoids. Scale bars, 50 μm. (**J** and **L**) Quantification of TBR1- and SATB2-labeled neurons in cerebral organoids. $N = 30$ cortex-like structures from 12 organoids of three independent lines. All data are represented as means ± SEM calculated with Student's *t* test. ns, not significant, $^{**}P < 0.01$, $^{***}P < 0.001$, and $^{****}P < 0.0001$.

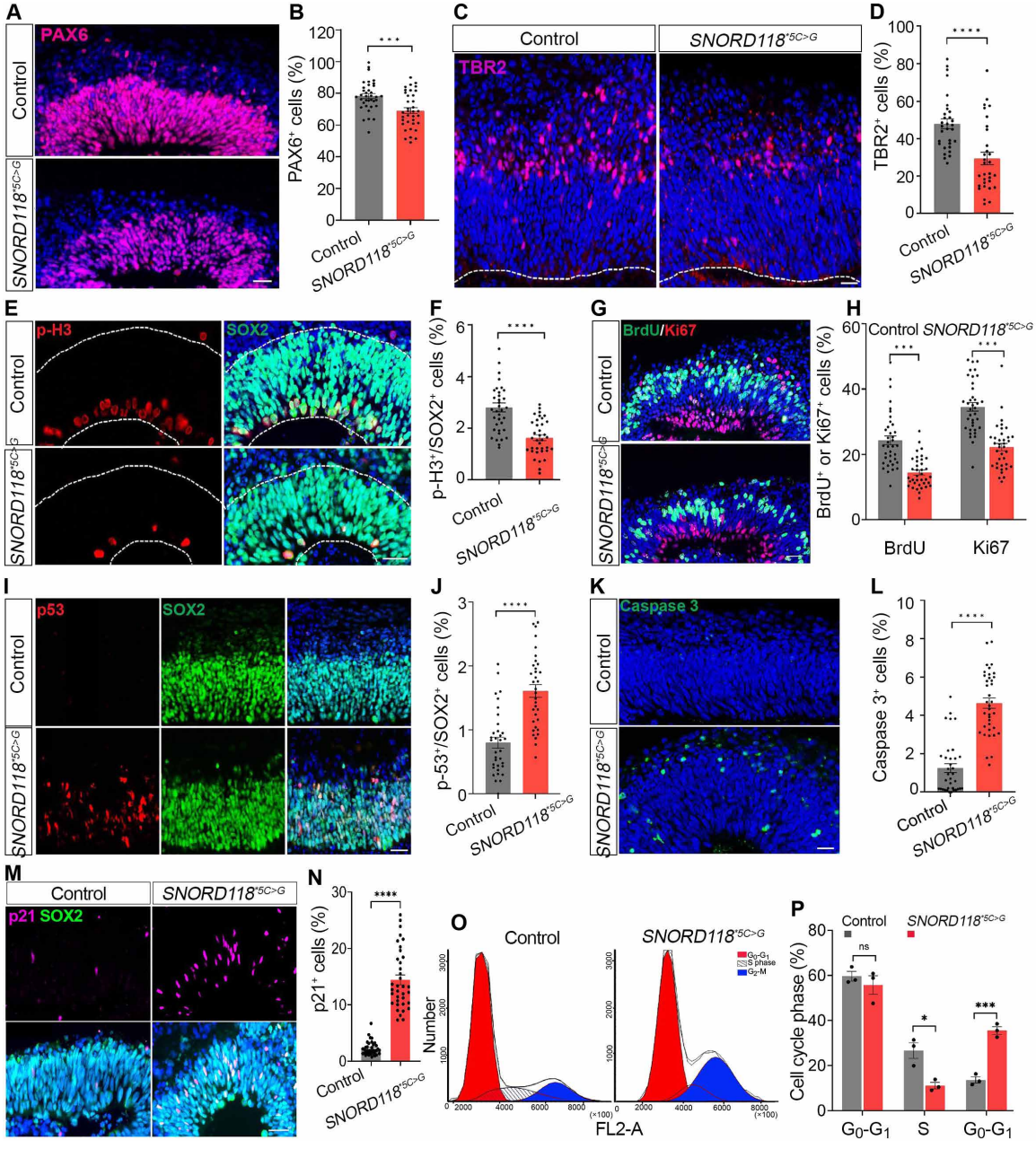

Fig. 2. Ribosomopathy hallmark cellular defects lead to reduced NPCs in *SNORD118*-mutant cerebral organoids. (**A** and **C**) Immunofluorescent staining of PAX6 and TBR2 in control and *SNORD118*$^{*5C>G}$ homozygous-mutant cerebral organoids. Scale bars, 50 μm. (**B** and **D**) Quantification of PAX6- and TBR2-labeled NPCs in cerebral organoids. (**E** and **G**) Immunofluorescent staining of p-H3 (red) and SOX2 (green), as well as BrdU (green) and Ki67 (red), in cerebral organoids. Scale bars, 50 μm. (**F** and **H**) Quantification of the percentage of p-H3;SOX2-, BrdU-, or Ki67-positive cells in cerebral organoids. (**I** and **K**) Immunofluorescent staining of p53 (red), SOX2 (green), or Caspase 3 (green) in cerebral organoids. Scale bars, 50 μm. (**J** and **L**) Quantification of p53- or Caspase 3–positive cells in the cortex-like structure of cerebral organoids. (**M**) Immunostaining of p21 (pink) and SOX2 (green) in human iPSC-derived cerebral organoids. Scale bar, 50 μm. (**N**) Quantification of the percentage of p21-positive cells in cerebral organoids. For all organoids. $N = 35$ to 37 cortex-like structures were obtained from 12 organoids, originating from three independent cell lines. (**O**) Cell cytometry analysis of cell cycle for NPCs. (**P**) Quantification of individual cell cycle phase. All data are represented as means ± SEM calculated by Student's *t* test. $^{*}P < 0.05$, $^{***}P < 0.001$, and $^{****}P < 0.0001$.

controls (Fig. 2, O and P). Thus, G_2 cell cycle arrest occurs in mutant NPCs. Together, *SNORD118*$^{*5C>G}$ homozygous mutations cause p53 signaling activation, cell cycle arrest, and apoptosis in NPCs, which leads to reduced NPCs. Our *SNORD118*$^{*5C>G}$ mutant cerebral organoids recapitulate typical cellular defects in ribosomopathies, resulting in brain growth retardation.

Snord118-mutant mice display ribosomopathy-like defects

To investigate *Snord118* functions in vivo, we generated a conditional KO (cKO) mouse line carrying floxed alleles of *Snord118* (fig. S2A). To investigate *Snord118* functions in NPCs during brain development in vivo, we used *EMX1*-Cre line to drive Cre expression that begins at embryonic (E) 9.5 in the NPCs of dorsal neocortex (*32*), as evidenced by

the exclusive expression of tdTomato in the neocortex of *EMX1*-Cre, Ai14 mice (fig. S2B). *EMX1*-Cre;*Snord118*$^{f/+}$ male mice were crossed with *Snord118*$^{f/f}$ females, followed by the analyses of age-matched littermate wild type (WT), *EMX1*-Cre;*Snord118*$^{f/+}$ heterozygous (HET), and *EMX1*-Cre;*Snord118*$^{f/f}$ homozygous (HOM) mice at E14.5. There is a dose-dependent reduction of brain weights in *Snord118* HET and HOM KO brains compared to WT controls (Fig. 3, A and B). Similarly, the whole embryo weights are correspondingly reduced in heterozygous and homozygous mutants (fig. S2, C and D). Nissl-staining of E14.5 embryonic brains showed that *EMX1*-Cre;*Snord118*$^{f/+}$ heterozygous mice exhibited a significantly reduced cortex thickness, which is more severe in homozygous mutants (Fig. 3, C and D). All mutant mice were born normally with an expected Mendelian ratio, but the homozygous mutant mice cannot survive more than one month. Our analyses at postnatal day 20 (p20) showed that mutant mice have smaller brain sizes and body weights compared to WT controls in a dose-dependent manner (fig. S3, A to D). The Nissl staining of sagittal sections of p20 mouse brains showed that the homozygous KO mice lack most of the neocortex, hippocampus, and corpus callosum (fig. S3E). Therefore, *Snord118* mutations lead to brain growth defects in mice in vivo.

To determine the cellular basis of mutant brains, we performed IHC staining and examined NPCs in E14.5 embryonic brains. Compared to WT controls, *EMX1*-Cre;*Snord118*$^{f/+}$ heterozygous mice displayed a significant decrease in the percentage of Pax6-positive

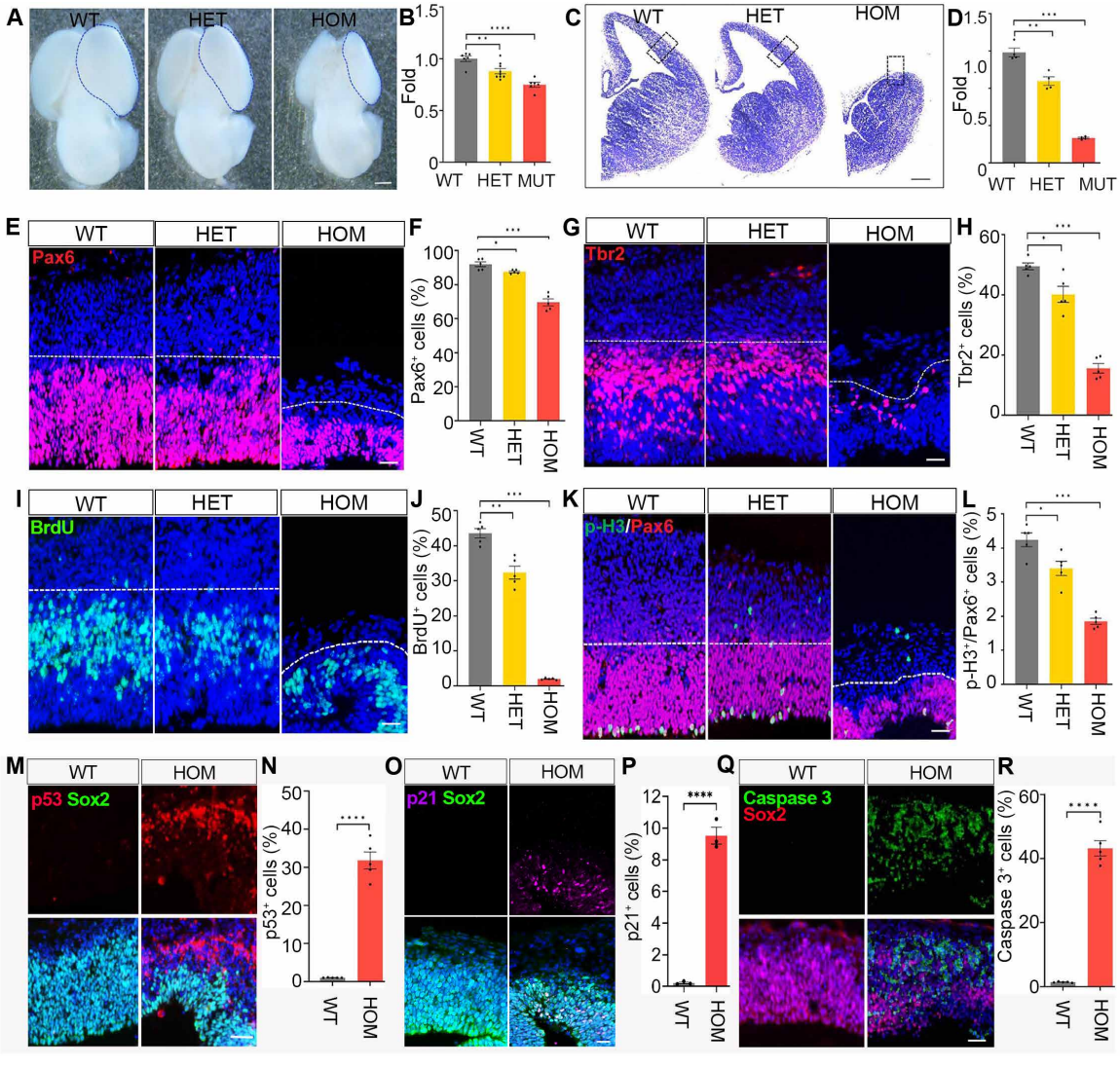

Fig. 3. Generate and characterize mouse models of *Snord118* ribosomopathy. (**A**) Dorsal views of E14.5 control, *EMX1*-Cre;*Snord118*$^{f/+}$ heterozygous (HET) and *EMX1*-Cre;*Snord118*$^{f/f}$ homozygous (HOM) mutant mouse brains. Scale bar, 1 mm. (**B**) Quantification of brain weights. $N = 6$ to 9 mice per group. (**C**) Nissl-staining of coronal sections of cerebral cortex. Scale bar, 200 μm. (**D**) Quantification of cerebral cortex thickness. $n = 4$ mice per group. (**E** and **G**) Immunofluorescent staining of Pax6 or Tbr2 in mouse cortex at E14.5. Scale bars, 50 μm. (**F** and **H**) Quantification of the percentage of Pax6-positive APCs and Tbr2-positive IPCs in mouse cortex. $n = 5$ mice for each group. (**I** and **K**) Immunofluorescent staining of BrdU, as well as p-H3 and Pax6 in mouse cortex. Scale bars, 50 μm. (**J** and **L**) Quantification of the percentage of BrdU- or p-H3;Pax6–positive cells in mouse cortex. $n = 5$ mice for each group. (**M**, **O**, and **Q**) Immunofluorescent staining of p53 (red) and Sox2 (green), p21 (pink) and Sox2 (green), as well as Caspase 3 (green) and Sox2 (red) in E12.5 mouse cortex. Scale bars, 50 μm. (**N**, **P**, and **R**) Quantification of the percentage of p53-, p21-, or Caspase 3–positive cells in mouse cortex. $n = 3$ or 5 mice for each group. All data are represented as means ± SEM calculated by one-way analysis of variance (ANOVA) with Tukey's post hoc tests or Student's *t* test. *$P < 0.05$, **$P < 0.01$, ***$P < 0.001$, and ****$P < 0.0001$.

APCs and Tbr2-positive IPCs, which are more severe in homozygous mutant mice (Fig. 3, E to H). To determine the causes of reduced NPCs, we examined cell cycle progression and cell proliferation. BrdU was used to monitor G_1-S phase transition. There was a significant decrease in the percentage of BrdU-positive NPCs in the VZ/SVZ regions in heterozygous and homozygous mutant brains (Fig. 3, I and J). The percentage of p-H3–positive APCs labeled by Pax6 was also reduced in mutant mice in a dose-dependent manner (Fig. 3, K and L). The p53 signaling is aberrantly up-regulated in the cerebral cortex of *Snord118* homozygous mutant embryonic brains (Fig. 3, M and N). We used p21 as a cell cycle arrest marker and found a significant increase in p21-positive NPCs labeled by Sox2 in mutant VZ/SVZ compared to controls (Fig. 3, O and P). Consequently, there is a significant increase in the percentage of Caspase 3–positive cells in the VZ/SVZ regions of homozygous mutant embryonic brains (Fig. 3, Q and R). Thus, *Snord118* KO mouse models exhibited NPC loss due to ribosomopathy-like cellular defects, including p53 activation, cell cycle arrest, and apoptosis.

SNORD118-mutant NPCs exhibit ribosome biogenesis and protein synthesis defects coupled with proteotoxicity

To investigate mechanisms underlying neurological defects in *SNORD118* ribosomopathy, we first examined U8 expression levels in hiPSC-derived cells, which were characterized by individual cell type markers (fig. S4, A to E). Our qPCR analysis showed that U8 is highly expressed in NPCs and cortical neurons compared to iPSCs, endothelial cells, pericytes, and microglia (Fig. 4A). This is consistent with phenotypes in mutant cerebral organoid and mouse models, which guide our mechanistic studies towards NPCs. Next, we attempted to identify its direct targets using our recently developed noncoding RNA target identification approach, named psoralen analysis of RNA interactions and structures (PARISs) (*33*). PARIS is a psoralen crosslinking-based method for high-throughput mapping of RNA duplexes in living cells at genome-wide levels with near base pair resolution (fig. S4F) (*33*). PARIS data revealed eight alternative conformations of U8 defined as Stemloops 1 to 8 (SL1 to SL8) in iPSC-derived NPCs (fig. S4G). The U8 target analysis showed that U8 binds to the 3′ end of the 28*S* rRNA as well as U13 snoRNA and *SNORD115* via base paring in human NPCs (fig. S4, H to J). To validate PARIS results, we synthesized U8 antisense oligonucleotides to pull down U8 in iPSC-NPCs, followed by qPCR analysis. In addition to 28*S*, U8 is confirmed to interact with U13, U35A, and *SNORD115* (fig. S4I).

The finding that U8 binds to 28S rRNA and other snoRNAs, key components in ribosome biogenesis, prompted us to examine rRNA maturation in *SNORD118*-mutant cells. We isolated RNAs from control and *SNORD118*$^{*5C>G}$ mutant hiPSC-derived NPCs followed by RNA electrophoresis in agarose. The quantification of the 28*S*:18*S* ratio showed that there is a reduced 28*S* rRNA in mutant NPCs compared to controls (Fig. 4, B and C), suggesting of rRNA maturation defects caused by *SNORD118* mutations. To measure rRNA synthesis, we performed a 5-ethynyl uridine (5-EU) incorporation assay (*34*). The intensity of 5-EU was decreased in mutant NPC nucleolus marked by Nucleophosmin 1 (NPM1) in vitro (Fig. 4, F and G). We also observed an in vivo reduction of 5-EU intensity in HET mouse cortex compared to WT cortex; 5-EU reduction is more pronounced in HOM than HET mouse cortex (Fig. 4, H and I). Thus, nucleolar transcriptional activity and rRNA synthesis are impaired due to *SNORD118*$^{*5C>G}$ mutations. The rRNA biogenesis impairment is expected to disrupt ribosome functions in protein synthesis. To measure protein synthesis, we performed *O*-propargyl-puromycin (OPP) incorporation assay, in which OPP acts as an analog of puromycin that enters the acceptor site of ribosomes and is incorporated into nascent polypeptides that can be detected by a click chemistry reaction (*35*). Control hiPSC-derived NPCs have a robust fluorescently labeled OPP, whose intensity is significantly reduced in *SNORD118*$^{*5C>G}$ mutant NPCs (Fig. 4, D and E). Therefore, *SNORD118* directly binds to rRNA and its loss in NPCs leads to impaired rRNA biogenesis and protein synthesis.

To investigate p53 activation mechanisms, we turned to RPL5/11–Mouse double minute 2 homolog (MDM2)–p53 signaling pathway. MDM2 is an E3 ubiquitin ligase and a suppressor of p53. When ribosomal biogenesis is impaired, extra RPs RPL5 and RPL11 bind to and sequester MDM2 leading to a reduced p53 suppression, resulting in p53 activation (*36*, *37*). Our immunoprecipitation of MDM2 found that there was an increased binding of RPL5 and RPL11 to MDM2 and a decreased binding between MDM2 and p53 in *SNORD118*$^{*5C>G}$ mutant NPCs (Fig. 4, J and K). Dysfunctions of ribosome biogenesis factors could result in aberrant ribosome assembly and the accumulation of orphan RPs, which elicit proteotoxic stress (*4*, *6*). Proteotoxic stress promotes the phosphorylation of eIF2 at serine-51 of the α subunit (eIF2α), triggering the ISR and leading to the decrease of global protein synthesis (*17*). Therefore, we used p-eIF2α to mark proteotoxic stress and observed that its intensity is significantly increased in *SNORD118*$^{*5C>G}$ mutant hiPSCs-derived NPCs compared to controls (Fig. 4, L and M). In addition to 2D culture NPCs, we next examined 3D cerebral organoids and similarly found that p-eIF2α is up-regulated in *SNORD118*$^{*5C>G}$ mutant cerebral organoids (Fig. 4, N and O). Therefore, *SNORD118* mutations activate RPL5/11-MDM2-p53 pathway and cause proteotoxic stress in addition to protein synthesis loss, which collectively lead to reduced proliferation in NPCs.

Small-molecule 2BAct mitigates ISR activation and ribosomopathy-like cellular defects in *SNORD118* mutant NPCs

Now, there are no effective treatments available for ribosomopathies. Our *SNORD118* mutant NPCs provide a large number of experimental materials with typical ribosomopathy-like cellular phenotypes, including protein synthesis loss, proteotoxicity, and p53 activation. Therefore, we used *SNORD118*-mutant human iPSC-derived NPCs and performed cell-based small-molecule screen for reversing proliferation defects in mutant NPCs. On the basis of published studies, we selected those chemical compounds that potentially affect ribosome biogenesis and nucleoli functions, including 2BAct (*38*), MCL-186 (*39*), bromosporine (*40*), nicotinamide (*41*), tideglusib (*42*, *43*), PFI-1 (*44*), YM201636 (*45*), cilostazol (*46*), leucine (*47*), and prostetin (*48*). Our initial EdU assay–based cell proliferation screen identified 2BAct, MCL-186, and cilostazol, which significantly increased the proliferation of *SNORD118*$^{*5C>G}$-mutant NPCs (Fig. 5, A and B). 2BAct is an improved version of small-molecule ISRIB (for ISR inhibitor) with highly selective, central nervous system (CNS)–permeable, and orally active features. It has been reported that 2BAct and ISRIB can repress ISR by dampening the up-regulation of p-eIF2α (*49*–*51*), which occurs in our mutant NPCs. The effects of 2BAct on ribosomopathies have not been examined. Therefore, we focused on 2BAct for the downstream analyses.

5-EU incorporation assay showed that 2BAct significantly improves rRNA synthesis, evidenced by an increased 5-EU intensity in 2BAct-treated *SNORD118*$^{*5C>G}$-mutant NPCs (Fig. 5, C and D). To verify 2BAct's effects on p-eIF2α in NPCs, we applied 2BAct to

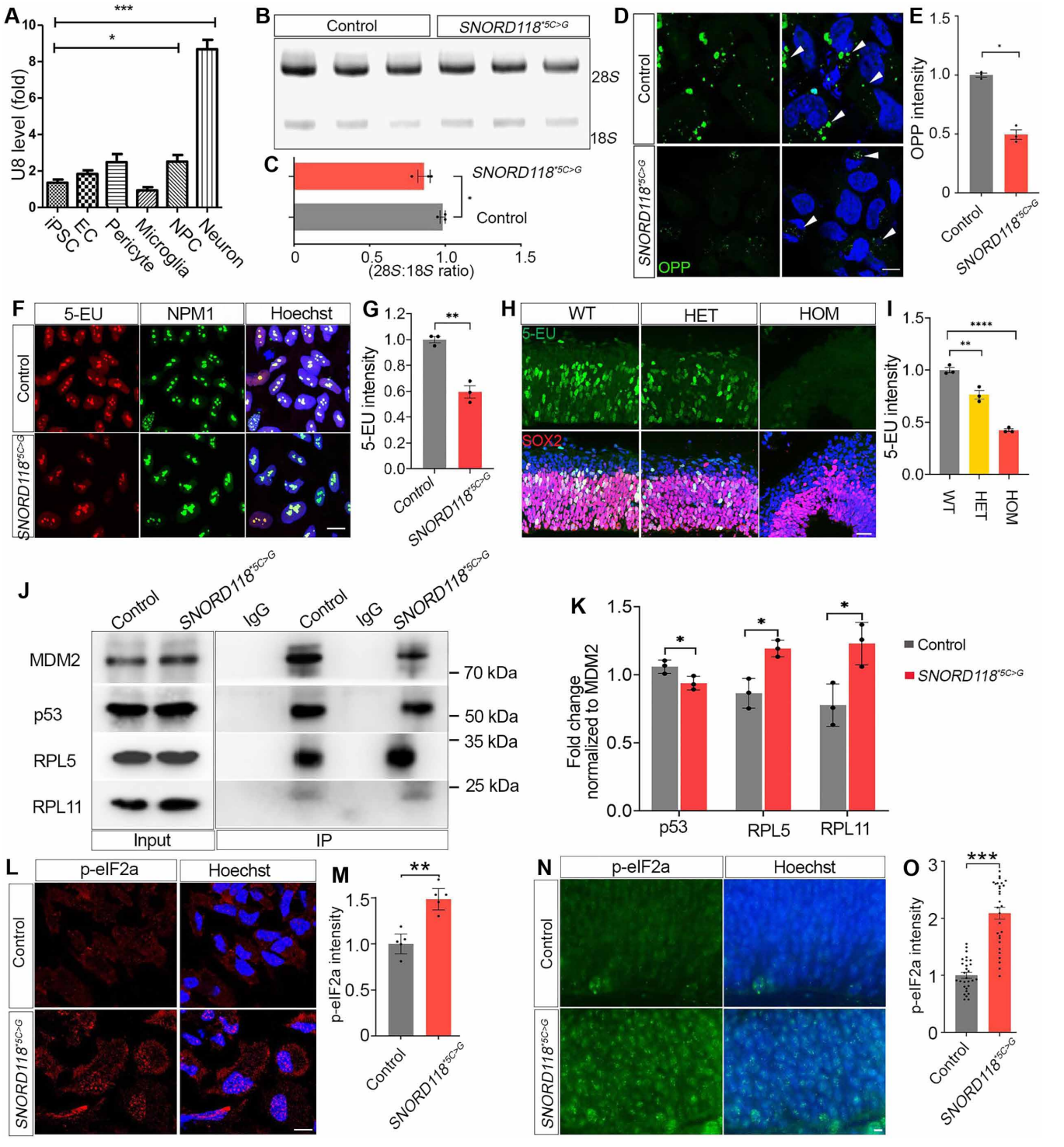

Fig. 4. Protein synthesis and proteotoxicity defects in *SNORD118*-mutant NPCs. (**A**) RT-PCR analysis of the expression levels of U8, encoded by *SNORD118*. (**B** and **C**) Agarose gel analysis of control and *SNORD118*$^{*5C>G}$ homozygous mutant NPCs, followed by the 28*S*:18*S* ratio measurements. (**D**) Representative images of fluorescently labeled O-propargyl-puromycin (OPP) in hiPSC-derived NPCs. White Arrowheads represent OPP incorporated into the cells. Scale bar, 10 μm. (**E**) Quantification of the relative OPP intensity. (**F**) 5-ethynyl uridine (5-EU) (red)–labeled iPSC-derived NPCs were costained with nucleolar marker NPM1 (green). Scale bar, 20 μm. (**G**) Quantification of the relative intensity of 5-EU in NPCs. (**H**) 5-EU incorporation in mouse embryonic cortex (E12.5) of WT, *EMX1*-Cre;*Snord118*$^{f/+}$ heterozygous (HET), and *EMX1*-Cre;*Snord118*$^{f/f}$ homozygous (HOM). Scale bar, 50 μm. (**I**) Quantification of the relative intensity of 5-EU in mouse NPCs. $N = 3$ mice. (**J**) Immunoprecipitation (IP) of control and *SNORD118*$^{*5C>G}$ iPSC-derived NPCs with MDM2 pull-down, followed by immunoblots for p53, RPL5, and RPL11. IgG, immunoglobulin G. (**K**) Quantification of blot intensities. $N = 3$ biological repeats. (**L** and **N**) Immunofluorescent staining of p-eIF2α staining in 2D NPCs or 3D cerebral organoids. Scale bars, 10 μm. (**M** and **O**) Quantification of p-eIF2α intensity. $N = 5$ in (M) and = 29 cortex-like structures from 12 organoids of three independent lines in (O). All data are represented as means ± SEM calculated by Student's *t* test. $^*P < 0.05$, $^{**}P < 0.01$, $^{***}P < 0.001$, and $^{****}P < 0.0001$.

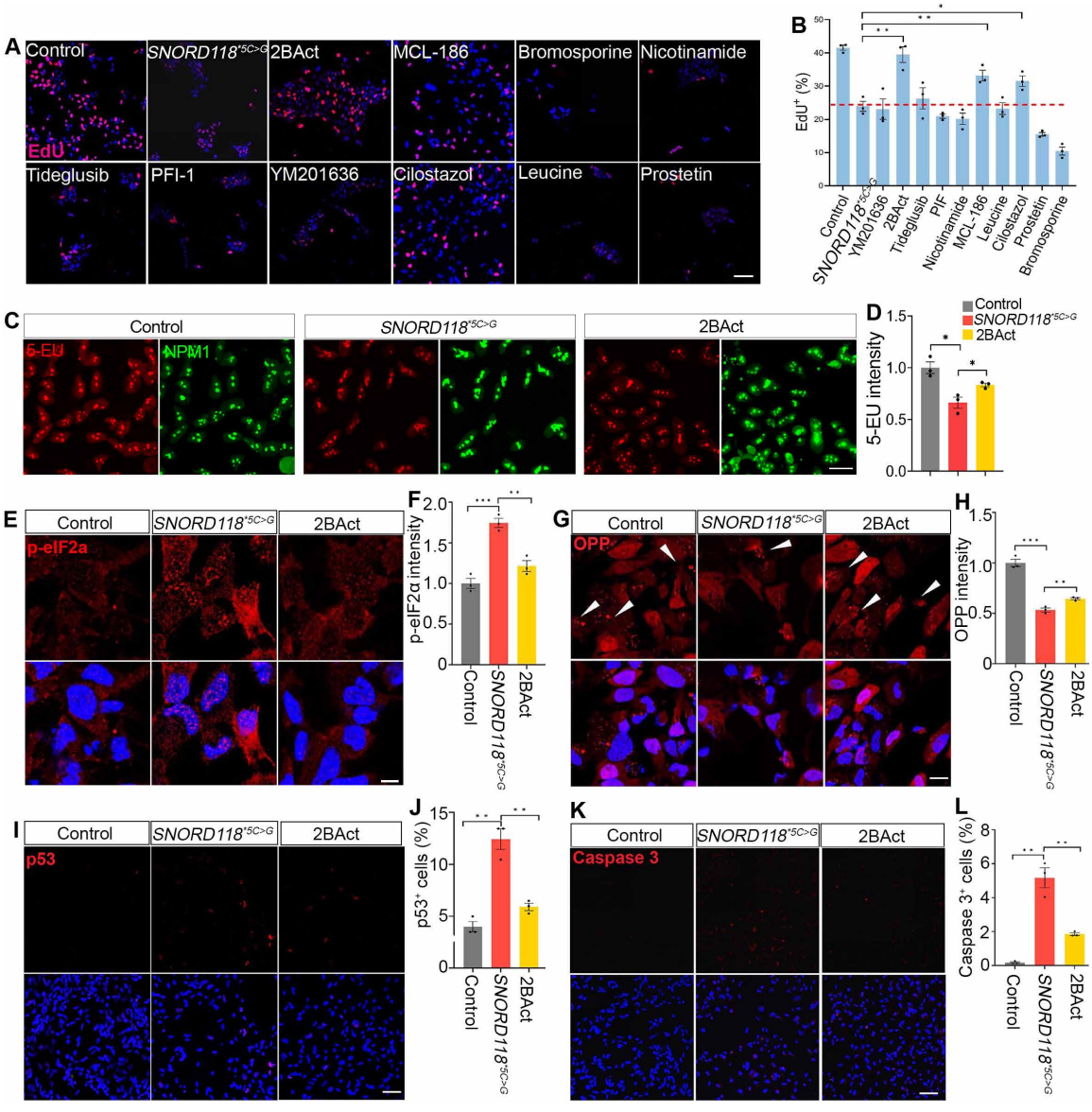

Fig. 5. 2BAct mitigates ribosomopathy-like cellular defects in mutant human iPSC-derived NPCs. (**A**) Representative images of EdU assay for small-molecule screening. Scale bar, 50 μm. (**B**) Quantification of the percentage of EdU-positive cells in control and treatment groups. PIF, prolactin inhibitory factor. (**C**) 5-EU (red) and NPM1 (green) staining in control and *SNORD118*$^{*5C>G}$ iPSC-derived NPCs with or without 2BAct treatment. Scale bar, 20 μm. (**D**) Quantification of the relative intensity of 5-EU. (**E**) Immunofluorescent staining of p-eIF2a. Scale bar, 20 μm. (**F**) Quantification of the relative p-eIF2a intensity. (**G**) Representative images of OPP assay. White arrowheads indicate the positive signals of OPP incorporated in the cells. Scale bar, 20 μm. (**H**) Quantification of relative OPP intensity. (**I** and **K**) Immunofluorescent staining of p53 and Caspase 3. Scale bars, 50 μm. (**J** and **L**) Quantification of the percentage of p53- and Caspase 3–positive cells. All data are represented as means ± SEM calculated by one-way ANOVA with Tukey's post hoc tests or Student's *t* test. **P* < 0.05, ***P* < 0.01, ****P* < 0.001, and *****P* < 0.0001.

SNORD118$^{*5C>G}$-mutant NPCs followed by immunostaining. 2BAct treatment significantly mitigated p-eIF2α intensity in mutant NPCs, which is nearly close to the levels in the control cells (Fig. 5, E and F). The p-eIF2α down-regulation is expected to release the global protein synthesis brake from ISR activation (*17*). OPP assay showed that the reduced protein synthesis in mutant NPCs is increased after 2BAct treatment (Fig. 5, G and H). It has been suggested that ribosomopathy defects are derived from ribosome loss and impaired protein synthesis, leading to disrupted mRNA translation and apoptosis (*2*, *3*). Therefore, to examine the functional significance of reversed protein synthesis by 2BAct treatment, we examined p53 activation in *SNORD118*-mutant NPCs with or without 2BAct treatment. Immunostaining showed that 2BAct treatment significantly reduced the percentage of p53-positive cells in the *SNORD118*$^{*5C>G}$ mutant NPCs (Fig. 5, I and J). Sustained p53 activation leads to cell apoptosis. Consistently, 2BAct treatment markedly reduced the percentage of Caspase 3–positive cells in mutant NPCs (Fig. 5, K and L). Together, these results suggest that p-eIF2α–mediated ISR activation is maladaptive, rather than cytoprotective, in *SNORD118*$^{*5C>G}$-mutant NPCs; ISR inhibition by 2BAct mitigates ribosomopathy hallmark defects.

2BAct mitigates neuronal fate and organoid growth defects in *SNORD118*-mutant cerebral organoids

To investigate the importance of 2BAct-mediated mitigation of ribosomopathy defects on brain development, we turned our attention to cerebral organoids. 2BAct were added to human iPSC-derived cells at the embryonic body (EB) stages during the generation of cerebral organoids (Fig. 6A). Then, 8-week-age organoids were examined and surface area analyses showed that 2BAct treatment can significantly increase the size of *SNORD118*$^{*5C>G}$-mutant cerebral organoids, which are smaller than control organoids (Fig. 6, B and C). To investigate the cellular mechanisms underlying the increased organoid size by 2BAct treatment, we used Ki67 to label all cycling cells followed by the analyses of VZ/SVZ-like cortical regions in the organoids. IHC staining showed that there is a significant increase of Ki67-positive cells in mutant organoids after 2BAct treatment (Fig. 6, D and E). We then used BrdU to mark G_1-S transition cells and found that 2BAct treatment rescued BrdU$^+$ cell reduction in the mutant organoids (Fig. 6, D and E). In parallel, we used p-H3 staining to label mitotic cells and found that 2BAct can significantly increase the percentage of p-H3–positive cells, which are reduced in mutants compared to control organoids (Fig. 6, F and G). To investigate how restored NPC behaviors by 2BAct affect neuronal production, we examined cortical layer neurons. Consistent with rescuing effects on NPC proliferation, 2BAct treatment significantly increased TBR1-positive neurons in mutant cerebral organoids (Fig. 6, H and I). Together, these results suggest that 2BAct is functionally important and can partially rescue neuronal cell fate and growth defects in *SNORD118*$^{*5C>G}$ cerebral organoids.

2BAct alleviates brain ribosomopathy defects in mice in vivo

To test in vivo rescuing effects of 2BAc, we crossed *EMX1*-Cre; *Snord118*$^{f/+}$ heterozygous males with *Snord118*$^{f/f}$ homozygous female mice and generated neural-specific *Snord118* cKO mice (refer to MUT mice here). The MUT and littermate WT mice were subjected to vehicle or 2BAct intraperitoneal daily injection from E11.5 to E15.5 (Fig. 7A). Brain weight analysis at E16.5 showed that 2BAct treatment significantly mitigated weight loss of *EMX1*-Cre;*Snord118*$^{f/f}$ mutant brains (Fig. 7, B and C). Histology analysis confirmed that MUT brains exhibited a markedly reduced cerebral cortex thickness, which is partially rescued by 2BAct treatment (Fig. 7, D and E). Consistent with cerebral organoid data, these results suggest that 2BAct treatment can rescue brain growth defects in *Snord118* cKO mice in vivo. To investigate the mechanisms underlying partially restored brain growth by 2BAct, we first examined how 2BAct influences the proteotoxicity in mutant brains by staining p-eIF2α. The IHC staining of cerebral cortex showed that 2BAct treatment significantly decreases the percentage of p-eIF2α–positive cells in cKO brains compared to vehicle controls (Fig. 7, F and G). Next, we examined the ribosomopathy hallmark defect, p53 activation, and found that 2BAct can markedly reduce the percentage of p53-positive cells in mutant cerebral cortex (Fig. 7, H and I). To further investigate the cellular effects of 2BAc in vivo, we performed BrdU labeling experiment and found that reduced BrdU-positive cells in mutant cerebral cortex were significantly increased by 2BAct treatment (Fig. 7, J and K). Consistent with increased proliferation and decreased p53 activation, there is a robust increase in the percentage of Pax6-positive APCs in mutant cerebral cortex after 2BAct

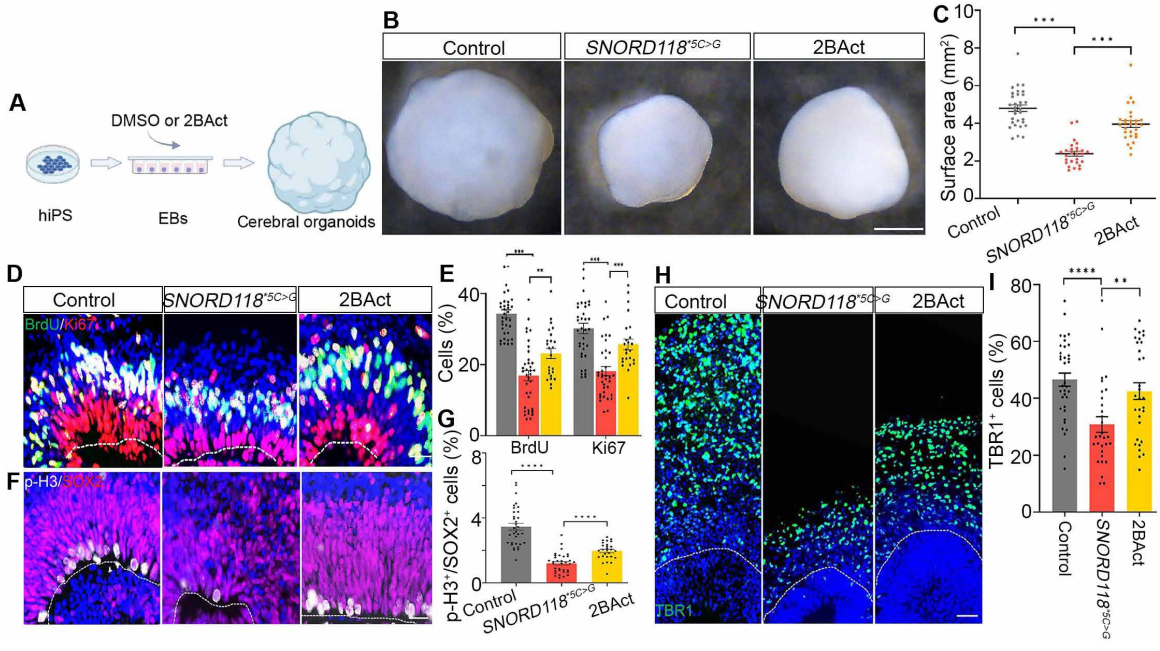

Fig. 6. 2BAct rescues neural cell fate and growth in mutant cerebral organoids. (**A**) Diagram of using dimethyl sulfoxide (DMSO) or 2BAct to treat cerebral organoids. (**B**) Bright-field images of 8-week control or *SNORD118*$^{*5C>G}$ cerebral organoids with or without treatment. Scale bar, 1 mm. (**C**) Quantification of surface areas of cerebral organoids. *N* = 27–32 organoids from three independent batches. (**D**) Immunofluorescent staining of BrdU (green) and Ki67 (red) in cerebral organoids. Scale bar, 20 μm. (**E**) Quantification of the percentage of BrdU- or Ki67-positive cells in the cerebral organoids. *N* = 24 to 36 cortex-like structures from 12 organoids in each group. (**F**) Immunofluorescent staining of p-H3 (white) and SOX2 (red) in cerebral organoids. Scale bar, 20 μm. (**G**) Quantification of the percentage of p-H3;SOX2–positive cells. *N* = 27 to 34 cortex-like structures from 12 organoids in each group. (**H**) Immunofluorescent staining of TBR1 in cerebral organoids. Scale bar, 50 μm. (**I**) Quantification of the percentage of TBR1-positive cells. *N* = 30 to 36 cortex-like structures from 12 organoids in each group. All data are represented as means ± SEM calculated by one-way ANOVA with Tukey's post hoc tests or Student's *t* test. $^{**}P < 0.01$, $^{***}P < 0.001$, and $^{****}P < 0.0001$.

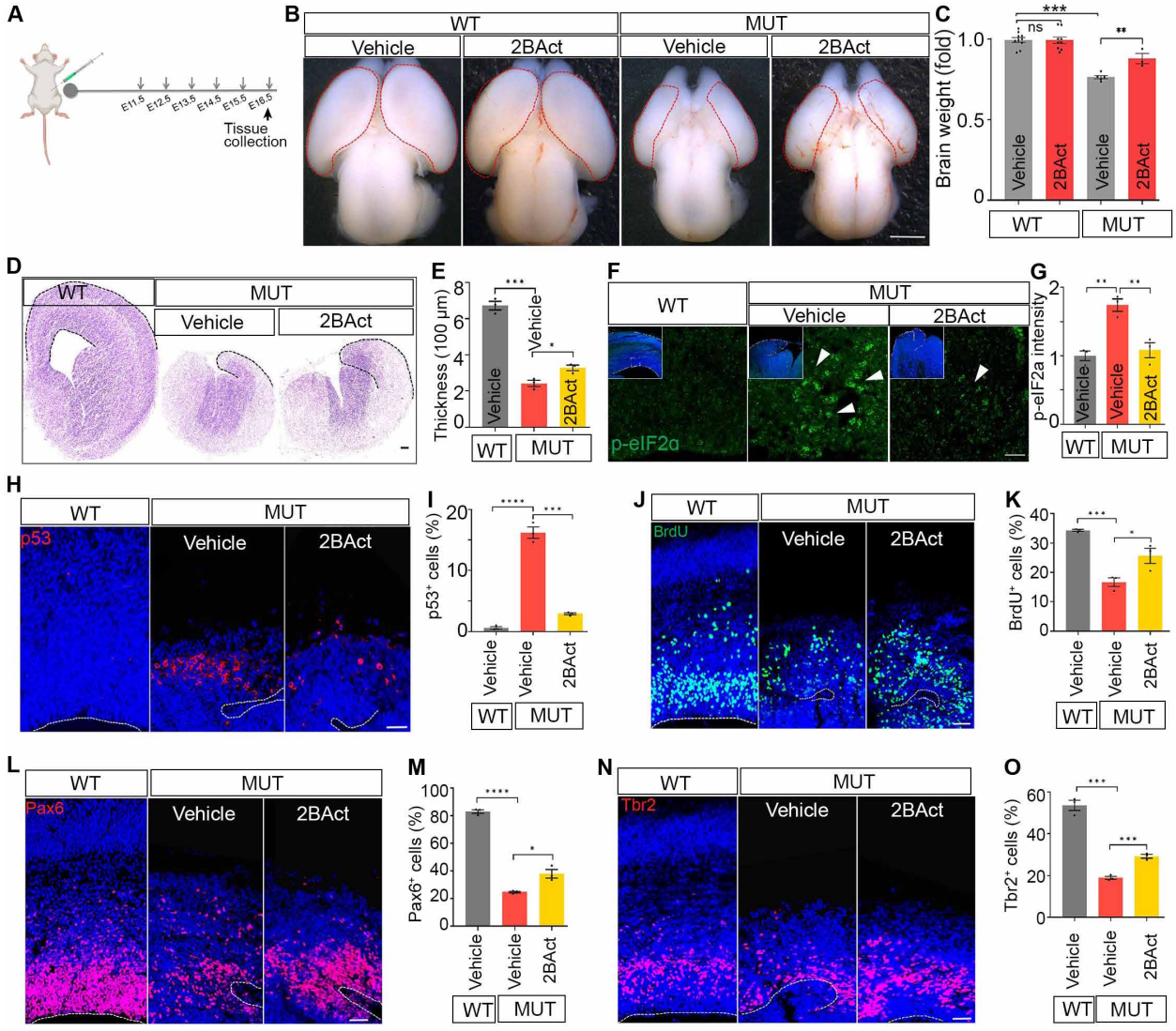

Fig. 7. 2BAct mitigates cellular and brain developmental defects in *Snord118* ribosomopathy mouse models in vivo. (**A**) Diagram of 2BAct injection for pregnant female mice from E11.5 to E15.5 with one dose (1.0 mg/kg) per day, followed by the embryo dissection at E16.5. (**B**) Bright-field images of vehicle and 2BAct-treated control and *EMX1-Cre;Snord118*$^{f/f}$ mouse brains. Scale bar, 1 mm. (**C**) Quantification of relative brain weights. $N = 3$ to 9 mice per group. (**D**) Nissl staining of brain sections. Dot lines indicate the cortex region. Scale bar, 100 μm. (**E**) Quantification of the cerebral cortex thickness. $N = 3$ mice in each group. (**F**) Immunofluorescent staining of p-eIF2a in the neocortex. Scale bar, 30 μm. (**G**) Quantification of relative p-eIF2a intensity in the neocortex. $N = 3$ mice in each group. (**H**, **J**, **L**, and **N**) Immunofluorescent staining of p53, BrdU, Pax6, or Tbr2 in the neocortex. Scale bars, 50 μm. (**I**, **K**, **M**, and **O**) Quantification of the percentage of p53-, BrdU-, Pax6-, or Tbr2-positive cells in the neocortex. $N = 3$ mice in each group. All data are represented as means ± SEM with statistical significance assessed by one-way ANOVA with Tukey's post hoc tests. $^*P < 0.05$, $^{**}P < 0.01$, $^{***}P < 0.001$, and $^{****}P < 0.0001$.

treatment (Fig. 7, L and M). Last, we showed that 2BAct treatment can significantly increase the percentage of Tbr2-positive IPCs in mutant cerebral cortex (Fig. 7, N and O). Together, these results suggest that 2BAct can alleviate brain ribosomopathy defects in *Snord118* cKO mice in vivo.

DISCUSSION

Using our newly generated cerebral organoid and mouse models of *Snord118* ribosomopathies, we identified maladaptive ISR as the key disease mechanism that drives ribosomopathy hallmark defects, including protein synthesis loss, p53 activation, and proteotoxic stress. Significantly, ISR inhibition by small-molecule 2BAct mitigated all evaluated brain defects in both organoid and mouse models of *Snord118* ribosomopathies, representing a new therapeutic strategy for treating ribosomopathies.

We generated the first cerebral organoid and mouse models of ribosomopathies due to *Snord118* mutations. *Snord118* mutations cause protein synthesis loss, p53 activation, proteotoxic stress, proliferation reduction, and cell death in NPCs, leading to brain growth retardation, which recapitulate symptoms in human leukoencephalopathy patients. Mouse models have been generated to recapitulate brain ribosomopathies such as leukodystrophies associated with mutations in RNA polymerase I (Pol I) or Pol III (*52*, *53*). Our and others' animal models

provide important opportunities for investigating disease mechanisms and therapeutic strategies. Human patient-derived *SNORD118*$^{*5C>G}$ homozygous mutations exhibited similar cellular defects as that in *SNORD118*$^{+/-}$ heterozygous mutations, suggesting a loss of function of U8 in *Snord118* ribosomopathies. Our *EMX1*-Cre–mediated *Snord118* neural-specific cKO mice developed ribosomopathy phenotypes, which resemble *Snord118*$^{*5C>G}$ homozygous mutant cerebral organoids. Therefore, the neural cell is a key cell type that is selectively affected by *Snord118*-mediated global disruption of ribosome biogenesis. This is consistent with the notion that specific cells are more sensitive to global perturbations in ribosome concentration (*1*, *2*). We found that *Snord118* is highly expressed in NPCs and cortical neurons compared to other cell types. Recent studies showed that a dynamic spatiotemporal activity of Pol I subunit is particularly important for neural crest cells (*54*). Together, these studies support a cell type–dependent ribosome concentration model for ribosomopathies (*7*).

Our study provides mechanistic insights underlying ribosomopathies. First, numerous ribosomopathy studies have confirmed that "ribosome stress" merges on p53 signaling, leading to cell cycle arrest and apoptosis (*5*, *55*). However, the upstream regulators of p53 activation remain incompletely understood. We demonstrated that p-eIF2α up-regulation–mediated ISR activation drives p53 signaling, as evidenced by the observation that ISR inhibition rescues p53 signaling and cell death in mutant cells. This finding echoes the connection between ribosome biogenesis, ribosome quality control, and ISR (*56*, *57*). In parallel, there was an increased binding of RPL5 and RPL11 to MDM2 and a decreased binding between MDM2 and p53 in *SNORD118*$^{*5C>G}$-mutant NPCs. RPL5 and RPL11 bind to and sequester MDM2, leading to less p53 suppression, which has been suggested as a critical step in p53 activation due to ribosomal biogenesis impairment (*36*, *37*). Our finding suggested that *SNORD118* mutation–mediated disruption in ribosome biogenesis resulted in increased RPL5 and RPL11 binding to MDM2. Therefore, less MDM2 are available to suppress p53, leading to p53 accumulation and cell apoptosis. Overall, nucleolar surveillance via RPL5/11-MDM2-p53 signaling pathway was activated in parallel with the ISR in *SNORD118*-mutant NPCs. Second, we found that ISR inhibition can reverse the protein synthesis loss in mutant cells. The p-eIF2α up-regulation–mediated inhibition of global protein synthesis could be an adaptive compensation response to the aberrant ribosome assembly or reduced ribosome numbers due to *Snord118* mutations. However, the prolonged p-eIF2α up-regulation ultimately becomes a pathological event leading to cell death. Restored protein synthesis and cell survival by ISR inhibitor 2BAct echoes the importance of ribosome and protein synthesis loss in driving ribosomopathy phenotypes (*2*, *3*). Third, our results suggest that ISR activation is maladaptive, instead of cytoprotective, in ribosomopathies. Our ISR inhibition mitigated all evaluated ribosomopathy-like phenotypes in *Snord118*-mutant organoids and mice at the molecular, cellular, and organ levels. Recent studies in the *Drosophila* model of ribosomopathy suggested that ISR plays a cytoprotective role (*4*). The discrepancy between our and *Drosophila* studies could be caused by differences in model systems, gene mutations, experimental tissues, or analyzed timing. Our studies suggest that p-eIF2α up-regulation–mediated ISR activation is a key driving factor for major ribosomopathy defects, including protein synthesis loss, p53 activation, and cell death.

We identified 2BAct-mediated targeting of ISR as a therapeutic strategy for treating *Snord118* ribosomopathies. So far, there are no effective therapies to treat ribosomopathies. Nutritional supplements L-leucine and antioxidants have been used in attempts to mitigate cellular defects in ribosomopathies with limited success (*58*, *59*). Here, we showed that pharmacological small-molecule drug 2BAct can rescue both protein synthesis and proteotoxicity defects and mitigate abnormalities of NPC fates and brain development in cerebral organoid and mouse models of *Snord118* ribosomopathies. 2BAct was selected from our small-molecule screening using human iPSC-derived NPCs and cerebral organoids. For the first time, our study links 2BAct with ribosomopathies. Small-molecule ISRIB (for ISR inhibitor) has been shown to provide beneficial effects in a wide range of diseases exhibiting maladaptive ISR (*49*–*51*). 2BAct is an improved version of ISRIB, and it functions as a highly selective, CNS-permeable, and orally active eIF2B activator. 2BAct has demonstrated functions in boosting eIF2B complex activity and in ameliorating ISR (*38*, *60*). Our studies further validated 2BAct's effective effects on ISR inhibition in mouse models of ribosomopathy in vivo. In addition, we should be cautious when extrapolating the findings from animal models into human diseases due to species differences (*61*, *62*), since promising drugs in animals frequently fail in the treatment of human diseases. In this regard, it is encouraging to see that our 2BAct treatment mitigated ribosomopathy defects in cerebral organoid-based human brain tissues. We anticipate that 2BAct could have a broad effect across the range of mutations identified in *SNORD118* ribosomopathy patient population. The degree of disease phenotype amelioration likely depends on the extent of cell and tissue damages in brains at the start of treatment. The brain defects, in turn, are determined by the specific *SNORD118* mutant alleles and disease onset time. Overall, 2BAct represents a potential therapeutic strategy for ribosomopathies by targeting ISR, a maladaptive brake on protein synthesis.

MATERIALS AND METHODS

Snord118 cKO mouse generation

The *Snord118* flox mouse was generated by Cyagen Biosciences. The *Snord118* exon was flanked via CRISPR-Cas9 by a loxP-exon-neo-loxP sequence. Targeted ES cell clones N-1B7 and N-1E9 were injected into C57BL/6 albino embryos, which were then re-implanted into CD-1 pseudo-pregnant females. Founder animals were identified by their coat color, and germline transmission was confirmed by breeding with C57BL/6 females and subsequent genotyping of the offspring. Three male and three female heterozygous-targeted mice were generated from clone N-1B7, and one male and one female heterozygous targeted mice were generated from clone N-1E9 as final deliverables for this project. The homozygous *Snord118* mice were mated with neural-specific *EMX1*-Cre (#005628, the Jackson laboratory) to generate cKO mice. All animals were handled according to protocols approved by the Institutional Animal Care and Use Committee at the University of Southern California.

Human iPSC culture

The human iPSC lines were characterized and obtained from National Institute of Neurological Disorders and Stroke Human Cell and Data Repository. The hiPSCs were cultured in mTeSR-plus medium (STEMCELL Technologies, 100-0276) and seeded on Geltrex (Thermo Fisher Scientific, A1413301)–coating culture dish. The hiPSCs were detached from the dish by incubation with ReLeSR (STEMCELL Technologies, 05872) for 1 min at room temperature (RT) followed by 5 min in a 37°C incubator. The cells were then dissociated into small cell clusters by manual pipetting. The medium was changed every other day.

Genome editing

The guide RNAs (gRNAs) were designed using the online software CHOPCHOP (https://chopchop.cbu.uib.no/) and cloned into pSpCas9 (BB)-2A-Puro (PX459) V2.0 vector. The gRNA-1: (5′-ATTTGC CTGTATCGTCAGGT-3′) was used for the generation of *Snord118* heterozygote KO hiPSCs. The gRNA-2 (5′-ATCGTCAGAAAGAAT CAGAT-3′) was used to generate the *Snord118*$^{*5C>G}$ point mutation hiPSCs. Briefly, hiPSCs were treated with ROCK inhibitor Y27632 (10 μM; Selleckchem) for 24 hours before electroporation. The cells were dissociated into single cells using Accutase cell detachment solution (Millipore, SCR005). A 10 μg of plasmid (with or without 1 μl of 100 uM ssODN for point mutation) was electroporated into 1.0×10^6 cells using NEPA21 Electro-Kinetic Transfection Systems, then immediately seeded on Geltrex-coated plates, and cultured in mTeSR-plus medium containing Y27632 (50 μM) for the first 24 hours. Puromycin (0.5 ug/ml) was added to the medium for 2 days selection. Then, hiPSCs were maintained in a medium without puromycin until colonies emerged. Individual colonies were picked up and expanded. PCR products were amplified and subjected to Sanger sequencing to identify mutant clones. The ssODN and primers used for hiPSCs genotyping were listed in table S1.

Human NPC generation

The hiPSCs were cultured until 80% confluence and then passaged into cell aggregates to form EBs. These EBs underwent suspended culture for 2 weeks in a neural induction medium, which is consisted of N2B27 medium supplemented with dual Smad inhibitors SB431542 (10 μM) and LDN-193189 (0.1 μM) (Selleckchem). N2B27 medium was 50% Dulbecco's modified Eagle's medium (DMEM)/F12, 50% neurobasal medium, 0.5% N2 supplement, 1% Gem21 supplement, 1% GlutaMAX, 0.2% primocin, and 1% nonessential amino acid (NEAA;Thermo Fisher Scientific). EBs were attached to the Geltrex-coated plates and cultured in a neural induction medium containing basic fibroblast growth factor (bFGF) (20 ng/ml) until the neural rosettes emerged. Neural rosettes were manually picked up and dissociated into individual cells by Accutase, which were then plated on Geltrex-coated plates. The NPCs were maintained in an N2B27 medium with bFGF (20 ng/ml) and epidermal growth factor (20 ng/ml), and the medium was changed every other day.

Generation of cerebral organoids

Cerebral organoid generation followed the published protocol with minor modifications (*29*, *63*). Briefly, hiPSC colonies were dissociated into single cells using Accutase. On day 1, a total of 9000 cells were plated into each well of an ultralow-attachment 96-well plate (Thermo Fisher Scientific) for single EB formation. The EB formation medium consisted of DMEM/F12, 20% KO serum replacement, 1% GlutaMAX, 1% NEAA, 50 μM Y27632, and bFGF (4 ng/ml; PeproTech). On day 4, EBs were cultured in an EB formation medium without Y27632 and bFGF. On day 7, EBs were cultured in a neural induction medium for 5 days. The neural induction medium is consisted of DMEM/F12, 0.5% N2 supplement, 1% GlutaMAX, 1% nonessential amino acids, 1% penicillin-streptomycin, and heparin (10 μg/ml) with dual Smad inhibitors A83-01(1 μM) and LDN-193189 (0.1 μM). On day 12, EBs were embedded into Geltrex droplets and cultured for 4 days in a medium containing 50% DMEM/F12, 50% neurobasal medium, 0.5% N2 supplement, 1% Gem21 supplement without vitamin A, 1% GlutaMAX, 1% NEAA, 0.2% primocin, and human insulin solution (2.5 ng/ml; Sigma-Aldrich). On day 16, organoids were transferred to a spinner flask rotating continuously at 60 rpm and cultured in an N2B27 medium with human insulin (2.5 ng/ml). The medium was changed every week.

Real-time qPCR

Total RNAs were extracted using an RNeasy Mini Kit (QIAGEN, 74104). The reverse transcription was performed using random primers and M-MLV Reverse Transcriptase (Promega, M1701). Quantitative RT-PCR analysis was performed using Ssofast EvaGreen supermix (Bio-Rad) and detected with Bio-Rad CFX96 Optics Module qPCR/reverse transcription PCR Thermal Cycler. The data were analyzed using the comparative CT (2-ΔΔCT) method. The ΔCT was calculated using β-actin as the internal control. All experiments were performed with three biological replicates. Primer sequences were provided in table S1.

Immunostaining staining

For human NPC immunostaining, cells were fixed in 4% paraformaldehyde (PFA) for 15 min at RT, washed twice with Dulbecco's phosphate-buffered saline (DPBS), and then incubated with primary antibodies in blocking buffer (2% goat serum +1% BSA + 0.1% Triton X-100 in DPBS) overnight at 4°C before secondary antibody incubation. Cerebral organoids were fixed in 4% PFA for 30 min at room temperature. Cerebral organoids were washed three times with DPBS, incubated in 30% sucrose solution at 4°C overnight, and then embedded in O.C.T. solution followed by dry ice freezing. The frozen cerebral organoids were sectioned into 10-μm-thick slices for immunostaining. Histological processing and IHC labeling of cryosections were performed using cerebral cortex sections from different stages of embryos as described previously. The primary antibodies are listed in table S2. The secondary antibodies used were Alexa 488, Alexa 568, and Alexa 647 conjugated to specific immunoglobulin G types (Invitrogen Molecular Probes).

BrdU labeling and EdU assay

E14.5 pregnant mice were injected intraperitoneally with BrdU (Sigma-Aldrich) at 25 mg/kg of body weight. The animals were euthanized 30 min after the injection. The embryo brains were dissected out and fixed in 4% PFA for 1.5 hours on ice. Subsequently, brains were stored in 30% sucrose overnight and embedded in the optimal cutting temperature (OCT) solution. For in vitro labeling, cerebral organoids were incubated in the medium containing BrdU (100 μM) for 2 hours in the CO_2 incubator at 37°C. Then, cerebral organoids were washed by DPBS and fixed in 4% PFA for 30 min at RT. The samples were stained with BrdU antibody after sectioning. The BrdU-positive cells were counted by ImageJ software. EdU assay was performed using the Click-&-Go EdU Cell Proliferation Assay Kit.

OPP incorporation assay

OPP assay was performed using Click-&-Go Plus OPP Protein Synthesis Assay Kits. Briefly, the cells were treated with OPP (20 μM) for 20 min, fixed with 4% PFA at RT for 15 min, and then incubated with 0.5% Triton X-100 in PBS for 20 min. The OPP was detected by the reaction cocktail following the manual. Last, cells were stained with Hoechst 33342. The OPP intensity of cells was measured by ImageJ software.

Psoralen analysis of RNA interactions and structures

The PARIS was performed following the published method (*33*). Briefly, cells were cross-linked by AMT (Sigma-Aldrich, A4330) and

were subjected to Stratalink 2400 UV crosslinker for 30 min under UV365 nm. The crosslinked RNAs were extracted using TRIzol reagent and RNeasy Mini kit (QIAGEN, 74104), according to the manufacturer's instructions. Antisense oligos targeting U8 were designed by ChIRP Probe Designer, and the biotinylated oligos were ordered from IDT. Streptavidin C1 Dynabeads (Invitrogen, 65002) were used to pull down the RNA-probe complex, which were fragmented using ShortCut RNase III (NEB, M0245). Then, proximity-ligated RNA fragments were subjected to the reverse crosslinking. Then, RNAs were ligated with the adaptor followed by the reverse transcription using SSIV (Invitrogen, 18090010). The cDNA were circularized by CircLigase II ssDNA Ligase and used for library construction and sequencing.

Supplementary Materials

This PDF file includes:

Supplementary methods
Figs. S1 to S4
Tables S1 to S4

REFERENCES AND NOTES

1. P. C. Yelick, P. A. Trainor, Ribosomopathies: Global process, tissue specific defects. *Rare Dis.* **3**, e1025185 (2015).
2. E. W. Mills, R. Green, Ribosomopathies: There's strength in numbers. *Science* **358**, eaan2755 (2017).
3. R. K. Khajuria, M. Munschauer, J. C. Ulirsch, C. Fiorini, L. S. Ludwig, S. K. McFarland, N. J. Abdulhay, H. Specht, H. Keshishian, D. R. Mani, M. Jovanovic, S. R. Ellis, C. P. Fulco, J. M. Engreitz, S. Schütz, J. Lian, K. W. Gripp, O. K. Weinberg, G. S. Pinkus, L. Gehrke, A. Regev, E. S. Lander, H. T. Gazda, W. Y. Lee, V. G. Panse, S. A. Carr, V. G. Sankaran, Ribosome Levels Selectively Regulate Translation and Lineage Commitment in Human Hematopoiesis. *Cell* **173**, 90–103.e19 (2018).
4. C. Recasens-Alvarez, C. Alexandre, J. Kirkpatrick, H. Nojima, D. J. Huels, A. P. Snijders, J.-P. Vincent, Ribosomopathy-associated mutations cause proteotoxic stress that is alleviated by TOR inhibition. *Nat. Cell Biol.* **23**, 127–135 (2021).
5. K. E. Sloan, M. T. Bohnsack, N. J. Watkins, The 5S RNP Couples p53 Homeostasis to Ribosome Biogenesis and Nucleolar Stress. *Cell Rep.* **5**, 237–247 (2013).
6. B. W. Tye, N. Commins, L. V. Ryazanova, M. Wühr, M. Springer, D. Pincus, L. S. Churchman, Proteotoxicity from aberrant ribosome biogenesis compromises cell fitness. *eLife* **8**, e43002 (2019).
7. S. Xue, M. Barna, Specialized ribosomes: A new frontier in gene regulation and organismal biology. *Nat. Rev. Mol. Cell Biol.* **13**, 355–369 (2012).
8. S. Lodato, P. Arlotta, Generating Neuronal Diversity in the Mammalian Cerebral Cortex. *Annu. Rev. Cell Dev. Biol.* **31**, 699–720 (2015).
9. J. C. Silbereis, S. Pochareddy, Y. Zhu, M. Li, N. Sestan, The cellular and molecular landscapes of the developing human central nervous system. *Neuron* **89**, 248–268 (2016).
10. A. A. Pollen, A. Bhaduri, M. G. Andrews, T. J. Nowakowski, O. S. Meyerson, M. A. Mostajo-Radji, E. D. Lullo, B. Alvarado, M. Bedolli, M. L. Dougherty, I. T. Fiddes, Z. N. Kronenberg, J. Shuga, A. A. Leyrat, J. A. West, M. Bershteyn, C. B. Lowe, B. J. Pavlovic, S. R. Salama, D. Haussler, E. E. Eichler, A. R. Kriegstein, Establishing Cerebral Organoids as Models of Human-Specific Brain Evolution. *Cell* **176**, 743–756.e17 (2019).
11. M. A. Lancaster, M. Renner, C.-A. Martin, D. Wenzel, L. S. Bicknell, M. E. Hurles, T. Homfray, J. M. Penninger, A. P. Jackson, J. A. Knoblich, Cerebral organoids model human brain development and microcephaly. *Nature* **501**, 373–379 (2013).
12. E. D. Lullo, A. R. Kriegstein, The use of brain organoids to investigate neural development and disease. *Nat. Rev. Neurosci.* **18**, 573–584 (2017).
13. M. Guzman-Ayala, M. Sachs, F. M. Koh, C. Onodera, A. Bulut-Karslioglu, C.-J. Lin, P. Wong, R. Nitta, J. S. Song, M. Ramalho-Santos, Chd1 is essential for the high transcriptional output and rapid growth of the mouse epiblast. *Development* **142**, 118–127 (2015).
14. S. Herrlinger, Q. Shao, M. Yang, Q. Chang, Y. Liu, X. Pan, H. Yin, L.-W. Xie, J.-F. Chen, Lin28-mediated promotion of protein synthesis is critical for neural progenitor cell maintenance and brain development in mice. *Development* **146**, dev173765 (2019).
15. K. F. Chau, M. L. Shannon, R. M. Fame, E. Fonseca, H. Mullan, M. B. Johnson, A. K. Sendamarai, M. W. Springel, B. Laurent, M. K. Lehtinen, Downregulation of ribosome biogenesis during early forebrain development. *eLife* **7**, e36998 (2018).
16. M. L. Kraushar, K. Thompson, H. R. S. Wijeratne, B. Viljetic, K. Sakers, J. W. Marson, D. L. Kontoyiannis, S. Buyske, R. P. Hart, M.-R. Rasin, Temporally defined neocortical translation and polysome assembly are determined by the RNA-binding protein Hu antigen R. *Proc. Natl. Acad. Sci. U. S. A.* **111**, E3815–E3824 (2014).
17. K. Pakos-Zebrucka, I. Koryga, K. Mnich, M. Ljujic, A. Samali, A. M. Gorman, The integrated stress response. *Embo Rep.* **17**, 1374–1395 (2016).
18. D. Ron, Translational control in the endoplasmic reticulum stress response. *J. Clin. Invest.* **110**, 1383–1388 (2002).
19. T. Kiss, E. Fayet, B. E. Jády, P. Richard, M. Weber, Biogenesis and Intranuclear Trafficking of Human Box C/D and H/ACA RNPs. *Cold Spring Harb. Symp. Quant. Biol.* **71**, 407–417 (2006).
20. G. A. Stepanov, J. A. Filippova, A. B. Komissarov, E. V. Kuligina, V. A. Richter, D. V. Semenov, Regulatory role of small nucleolar RNAs in human diseases. *Biomed. Res. Int.* **2015**, 206849 (2015).
21. J. Kufel, P. Grzechnik, Small Nucleolar RNAs Tell a Different Tale. *Trends Genet.* **35**, 104–117 (2019).
22. B. A. Peculis, J. A. Steitz, Disruption of U8 nucleolar snRNA inhibits 5.8S and 28S rRNA processing in the Xenopus oocyte. *Cell* **73**, 1233–1245 (1993).
23. B. A. Peculis, The sequence of the 5′ End of the U8 small nucleolar RNA is critical for 5.8S and 28S rRNA maturation. *Mol. Cell. Biol.* **17**, 3702–3713 (1997).
24. J.-L. Langhendries, E. Nicolas, G. Doumont, S. Goldman, D. L. J. Lafontaine, The human box C/D snoRNAs U3 and U8 are required for pre-rRNA processing and tumorigenesis. *Oncotarget* **7**, 59519–59534 (2016).
25. E. J. McFadden, S. J. Baserga, U8 variants on the brain: A small nucleolar RNA and human disease. *RNA Biol.* **19**, 412–418 (2022).
26. Y. J. Crow, H. Marshall, G. I. Rice, L. Seabra, E. M. Jenkinson, K. Baranano, R. Battini, A. Berger, E. Blair, T. Blauwblomme, F. Bolduc, N. Boddaert, J. Buckard, H. Burnett, S. Calvert, R. Caumes, A. C. Ng, D. Chiang, D. B. Clifford, D. M. Cordelli, A. Burca, N. Demic, I. Desguerre, L. D. Waele, A. D. Fonzo, S. R. Dunham, S. Dyack, F. Elmslie, M. Ferrand, G. Fisher, E. G. Karimiani, J. Ghoumid, F. Gibbon, H. Goel, H. T. Hilmarsen, I. Hughes, A. Jacob, E. A. Jones, R. Kumar, R. J. Leventer, S. MacDonald, R. Maroofian, S. G. Mehta, I. Metz, E. Monfrini, D. Neumann, M. Noetzel, M. O'Driscoll, K. Ounap, A. Panzer, S. Parikh, P. Prabhakar, F. Ramond, R. Sandford, R. Saneto, C. Soh, C. A. Stutterd, G. M. Subramanian, K. Talbot, R. H. Thomas, C. Toro, R. Touraine, E. Wakeling, E. Wassmer, A. Whitney, J. H. Livingston, R. T. O'Keefe, A. P. Badrock, Leukoencephalopathy with calcifications and cysts: Genetic and phenotypic spectrum. *Am. J. Med. Genet. A* **185**, 15–25 (2021).
27. E. M. Jenkinson, M. P. Rodero, P. R. Kasher, C. Uggenti, A. Oojageer, L. C. Goosey, Y. Rose, C. J. Kershaw, J. E. Urquhart, S. G. Williams, S. S. Bhaskar, J. O'Sullivan, G. M. Baerlocher, M. Haubitz, G. Aubert, K. W. Barañano, A. J. Barnicoat, R. Battini, A. Berger, E. M. Blair, J. E. Brunstrom-Hernandez, J. A. Buckard, D. M. Cassiman, R. Caumes, D. M. Cordelli, L. M. D. Waele, A. J. Fay, P. Ferreira, N. A. Fletcher, A. E. Fryer, H. Goel, C. A. Hemingway, M. Henneke, I. Hughes, R. J. Jefferson, R. Kumar, L. Lagae, P. G. Landrieu, C. M. Lourenço, T. J. Malpas, S. G. Mehta, I. Metz, S. Naidu, K. Ounap, A. Panzer, P. Prabhakar, G. Quaghebeur, R. Schiffmann, E. H. Sherr, K. R. Sinnathuray, C. Soh, H. S. Stewart, J. Stone, H. V. Esch, C. E. G. V. Mol, A. Vanderver, E. L. Wakeling, A. Whitney, G. D. Pavitt, S. Griffiths-Jones, G. I. Rice, P. Revy, M. S. van der Knaap, J. H. Livingston, R. T. O'Keefe, Y. J. Crow, Mutations in SNORD118 cause the cerebral microangiopathy leukoencephalopathy with calcifications and cysts. *Nat. Genet.* **48**, 1185–1192 (2016).
28. D. P. Leone, K. Srinivasan, B. Chen, E. Alcamo, S. K. McConnell, The determination of projection neuron identity in the developing cerebral cortex. *Curr. Opin. Neurobiol.* **18**, 28–35 (2008).
29. W. Zhang, S.-L. Yang, M. Yang, S. Herrlinger, Q. Shao, J. L. Collar, E. Fierro, Y. Shi, A. Liu, H. Lu, B. E. Herring, M.-L. Guo, S. Buch, Z. Zhao, J. Xu, Z. Lu, J.-F. Chen, Modeling microcephaly with cerebral organoids reveals a WDR62–CEP170–KIF2A pathway promoting cilium disassembly in neural progenitors. *Nat. Commun.* **10**, 2612 (2019).
30. F. Bunz, A. Dutriaux, C. Lengauer, T. Waldman, S. Zhou, J. P. Brown, J. M. Sedivy, K. W. Kinzler, B. Vogelstein, Requirement for p53 and p21 to Sustain G_2 Arrest After DNA Damage. *Science* **282**, 1497–1501 (1998).
31. L. Yiangou, R. A. Grandy, C. M. Morell, R. A. Tomaz, A. Osnato, J. Kadiwala, D. Muraro, J. Garcia-Bernardo, S. Nakanoh, W. G. Bernard, D. Ortmann, D. J. McCarthy, I. Simonic, S. Sinha, L. Vallier, Method to synchronize cell cycle of human pluripotent stem cells without affecting their fundamental characteristics. *Stem Cell Rep.* **12**, 165–179 (2019).
32. J. A. Gorski, T. Talley, M. Qiu, L. Puelles, J. L. R. Rubenstein, K. R. Jones, Cortical excitatory neurons and glia, but not GABAergic neurons, are produced in the Emx1-expressing lineage. *J. Neurosci.* **22**, 6309–6314 (2002).
33. Z. Lu, Q. C. Zhang, B. Lee, R. A. Flynn, M. A. Smith, J. T. Robinson, C. Davidovich, A. R. Gooding, K. J. Goodrich, J. S. Mattick, J. P. Mesirov, T. R. Cech, H. Y. Chang, RNA duplex map in living cells reveals higher-order transcriptome structure. *Cell* **165**, 1267–1279 (2016).
34. V. Prakash, B. B. Carson, J. M. Feenstra, R. A. Dass, P. Sekyrova, A. Hoshino, J. Petersen, Y. Guo, M. M. Parks, C. M. Kurylo, J. E. Batchelder, K. Haller, A. Hashimoto, H. Rundqivst, J. S. Condeelis, C. D. Allis, D. Drygin, M. A. Nieto, M. Andäng, P. Percipalle, J. Bergh, I. Adameyko, A.-K. Ö. Farrants, J. Hartman, D. Lyden, K. Pietras, S. C. Blanchard, C. T. Vincent, Ribosome biogenesis during cell cycle arrest fuels EMT in development and disease. *Nat. Commun.* **10**, 2110 (2019).
35. J. Liu, Y. Xu, D. Stoleru, A. Salic, Imaging protein synthesis in cells and tissues with an alkyne analog of puromycin. *Proc. Natl. Acad. Sci. U.S.A.* **109**, 413–418 (2012).

36. S. Bursać, M. C. Brdovčak, M. Pfannkuchen, I. Orsolić, L. Golomb, Y. Zhu, C. Katz, L. Daftuar, K. Grabušić, I. Vukelić, V. Filić, M. Oren, C. Prives, S. Volarević, Mutual protection of ribosomal proteins L5 and L11 from degradation is essential for p53 activation upon ribosomal biogenesis stress. *Proc. Natl. Acad. Sci.* **109**, 20467–20472 (2012).
37. M. A. E. Lohrum, R. L. Ludwig, M. H. G. Kubbutat, M. Hanlon, K. H. Vousden, Regulation of HDM2 activity by the ribosomal protein L11. *Cancer Cell* **3**, 577–587 (2003).
38. Y. L. Wong, L. LeBon, A. M. Basso, K. L. Kohlhaas, A. L. Nikkel, H. M. Robb, D. L. Donnelly-Roberts, J. Prakash, A. M. Swensen, N. D. Rubinstein, S. Krishnan, F. E. McAllister, N. V. Haste, J. J. O'Brien, M. Roy, A. Ireland, J. M. Frost, L. Shi, S. Riedmaier, K. Martin, M. J. Dart, C. Sidrauski, eIF2B activator prevents neurological defects caused by a chronic integrated stress response. *eLife* **8**, e42940 (2019).
39. H. Kawai, H. Nakai, M. Suga, S. Yuki, T. Watanabe, K. I. Saito, Effects of a novel free radical scavenger, MCI-186, on ischemic brain damage in the rat distal middle cerebral artery occlusion model. *J. Pharmacol. Exp. Ther.* **281**, 921–927 (1997).
40. A. Corman, B. Jung, M. Häggblad, L. Bräutigam, V. Lafarga, L. Lidemalm, D. Hühn, J. Carreras-Puigvert, O. Fernandez-Capetillo, A Chemical Screen Identifies Compounds Limiting the Toxicity of *C9ORF72* Dipeptide Repeats. *Cell Chem. Biol.* **26**, 235–243.e5 (2019).
41. D. C. Schöndorf, D. Ivanyuk, P. Baden, A. Sanchez-Martinez, S. D. Cicco, C. Yu, I. Giunta, L. K. Schwarz, G. D. Napoli, V. Panagiotakopoulou, S. Nestel, M. Keatinge, J. Pruszak, O. Bandmann, B. Heimrich, T. Gasser, A. J. Whitworth, M. Deleidi, The NAD+ Precursor Nicotinamide Riboside Rescues Mitochondrial Defects and Neuronal Loss in iPSC and Fly Models of Parkinson's Disease. *Cell Rep.* **23**, 2976–2988 (2018).
42. J. A. Morales-Garcia, R. Luna-Medina, S. Alonso-Gil, M. Sanz-SanCristobal, V. Palomo, C. Gil, A. Santos, A. Martinez, A. Perez-Castillo, Glycogen synthase kinase 3 inhibition promotes adult hippocampal neurogenesis in vitro and in vivo. *ACS Chem. Nerosci.* **3**, 963–971 (2012).
43. C. Fuchs, N. Fustini, S. Trazzi, L. Gennaccaro, R. Rimondini, E. Ciani, Treatment with the GSK3-beta inhibitor Tideglusib improves hippocampal development and memory performance in juvenile, but not adult, *Cdkl5* knockout mice. *Eur. J. Neurosci.* **47**, 1054–1066 (2018).
44. E. Quezada, C. Cappelli, I. Diaz, N. Jury, N. Wightman, R. H. Brown, M. Montecino, B. van Zundert, BET bromodomain inhibitors PFI-1 and JQ1 are identified in an epigenetic compound screen to enhance *C9ORF72* gene expression and shown to ameliorate *C9ORF72*-associated pathological and behavioral abnormalities in a C9ALS/FTD model. *Clin. Epigenetics* **13**, 56 (2021).
45. Y. Shi, S. Lin, K. A. Staats, Y. Li, W.-H. Chang, S.-T. Hung, E. Hendricks, G. R. Linares, Y. Wang, E. Y. Son, X. Wen, K. Kisler, B. Wilkinson, L. Menendez, T. Sugawara, P. Woolwine, M. Huang, M. J. Cowan, B. Ge, N. Koutsodendris, K. P. Sandor, J. Komberg, V. R. Vangoor, K. Senthilkumar, V. Hennes, C. Seah, A. R. Nelson, T.-Y. Cheng, S.-J. J. Lee, P. R. August, J. A. Chen, N. Wisniewski, V. Hanson-Smith, T. G. Belgard, A. Zhang, M. Coba, C. Grunseich, M. E. Ward, L. H. van den Berg, R. J. Pasterkamp, D. Trotti, B. V. Zlokovic, J. K. Ichida, Haploinsufficiency leads to neurodegeneration in C9ORF72 ALS/FTD human induced motor neurons. *Nat. Med.* **24**, 313–325 (2018).
46. N. V. Licata, R. Cristofani, S. Salomonsson, K. M. Wilson, L. Kempthorne, D. Vaizoglu, V. G. D'Agostino, D. Pollini, R. Loffredo, M. Pancher, V. Adami, P. Bellosta, A. Ratti, G. Viero, A. Quattrone, A. M. Isaacs, A. Poletti, A. Provenzani, C9orf72 ALS/FTD dipeptide repeat protein levels are reduced by small molecules that inhibit PKA or enhance protein degradation. *EMBO J.* **41**, e105026 (2022).
47. E. M. Payne, M. Virgilio, A. Narla, H. Sun, M. Levine, B. H. Paw, N. Berliner, A. T. Look, B. L. Ebert, A. Khanna-Gupta, L-leucine improves the anemia and developmental defects associated with Diamond-Blackfan anemia and del(5q) MDS by activating the mTOR pathway. *Blood* **120**, 2214–2224 (2012).
48. P. H. Bos, E. R. Lowry, J. Costa, S. Thams, A. Garcia-Diaz, A. Zask, H. Wichterle, B. R. Stockwell, Development of MAP4 Kinase Inhibitors as Motor Neuron-Protecting Agents. *Cell Chem. Biol.* **26**, 1703–1715.e37 (2019).
49. H. G. Nguyen, C. S. Conn, Y. Kye, L. Xue, C. M. Forester, J. E. Cowan, A. C. Hsieh, J. T. Cunningham, C. Truillet, F. Tameire, M. J. Evans, C. P. Evans, J. C. Yang, B. Hann, C. Koumenis, P. Walter, P. R. Carroll, D. Ruggero, Development of a stress response therapy targeting aggressive prostate cancer. *Sci. Transl. Med.* **10**, eaar2036 (2018).
50. A. Chou, K. Krukowski, T. Jopson, P. J. Zhu, M. Costa-Mattioli, P. Walter, S. Rosi, Inhibition of the integrated stress response reverses cognitive deficits after traumatic brain injury. *Proc. Natl. Acad. Sci. U.S.A* **114**, E6420–E6426 (2017).
51. C. Sidrauski, D. Acosta-Alvear, A. Khoutorsky, P. Vedantham, B. R. Hearn, H. Li, K. Gamache, C. M. Gallagher, K. K.-H. Ang, C. Wilson, V. Okreglak, A. Ashkenazi, B. Hann, K. Nader, M. R. Arkin, A. R. Renslo, N. Sonenberg, P. Walter, Pharmacological brake-release of mRNA translation enhances cognitive memory. *eLife* **2**, e00498 (2013).
52. E. Merheb, M.-H. Cui, J. C. DuBois, C. A. Branch, M. Gulinello, B. Shafit-Zagardo, R. D. Moir, I. M. Willis, Defective myelination in an RNA polymerase III mutant leukodystrophic mouse. *Proc. Natl. Acad. Sci. U.S.A* **118**, e2024378118 (2021).
53. M. A. Michell-Robinson, K. E. N. Watt, V. Grouza, J. Macintosh, M. Pinard, M. Tuznik, X. Chen, L. Darbelli, C.-L. Wu, S. Perrier, D. Chitsaz, N. A. Uccelli, H. Liu, T. C. Cox, C. W. Müller, T. E. Kennedy, B. Coulombe, D. A. Rudko, P. A. Trainor, G. Bernard, Hypomyelination, hypodontia and craniofacial abnormalities in aPolr3bmouse model of leukodystrophy. *Brain* **146**, 5070–5085 (2023).
54. K. T. Falcon, K. E. N. Watt, S. Dash, R. Zhao, D. Sakai, E. L. Moore, S. Fitriasari, M. Childers, M. E. Sardiu, S. Swanson, D. Tsuchiya, J. Unruh, G. Bugarinovic, L. Li, R. Shiang, A. Achilleos, J. Dixon, M. J. Dixon, P. A. Trainor, Dynamic regulation and requirement for ribosomal RNA transcription during mammalian development. *Proc. Natl. Acad. Sci. U.S.A* **119**, e2116974119 (2022).
55. A. Chakraborty, T. Uechi, N. Kenmochi, Guarding the 'translation apparatus': Defective ribosome biogenesis and the p53 signaling pathway. *Wiley Interdiscip Rev. RNA* **2**, 507–522 (2011).
56. A. C. Vind, A. V. Genzor, S. Bekker-Jensen, Ribosomal stress-surveillance: Three pathways is a magic number. *Nucleic Acids Res.* **48**, 10648–10661 (2020).
57. L. L. Yan, H. S. Zaher, Ribosome quality control antagonizes the activation of the integrated stress response on colliding ribosomes. *Mol. Cell* **81**, 614–628.e4 (2021).
58. J. Boultwood, B. H. Yip, C. Vuppusetty, A. Pellagatti, J. S. Wainscoat, Activation of the mTOR pathway by the amino acid l-leucine in the 5q- syndrome and other ribosomopathies. *Adv. Biol. Regul.* **53**, 8–17 (2013).
59. D. Sakai, J. Dixon, A. Achilleos, M. Dixon, P. A. Trainor, Prevention of Treacher Collins syndrome craniofacial anomalies in mouse models via maternal antioxidant supplementation. *Nat. Commun.* **7**, 10328 (2016).
60. Y. L. Wong, L. LeBon, R. Edalji, H. B. Lim, C. Sun, C. Sidrauski, The small molecule ISRIB rescues the stability and activity of Vanishing White Matter Disease eIF2B mutant complexes. *eLife* **7**, e32733 (2018).
61. R. M. Ransohoff, All (animal) models (of neurodegeneration) are wrong. Are they also useful? *J. Exp. Med.* **215**, 2955–2958 (2018).
62. R. D. Hodge, T. E. Bakken, J. A. Miller, K. A. Smith, E. R. Barkan, L. T. Graybuck, J. L. Close, B. Long, N. Johansen, O. Penn, Z. Yao, J. Eggermont, T. Höllt, B. P. Levi, S. I. Shehata, B. Aevermann, A. Beller, D. Bertagnolli, K. Brouner, T. Casper, C. Cobbs, R. Dalley, N. Dee, S.-L. Ding, R. G. Ellenbogen, O. Fong, E. Garren, J. Goldy, R. P. Gwinn, D. Hirschstein, C. D. Keene, M. Keshk, A. L. Ko, K. Lathia, A. Mahfouz, Z. Maltzer, M. McGraw, T. N. Nguyen, J. Nyhus, J. G. Ojemann, A. Oldre, S. Parry, S. Reynolds, C. Rimorin, N. V. Shapovalova, S. Somasundaram, A. Szafer, E. R. Thomsen, M. Tieu, G. Quon, R. H. Scheuermann, R. Yuste, S. M. Sunkin, B. Lelieveldt, D. Feng, L. Ng, A. Bernard, M. Hawrylycz, J. W. Phillips, B. Tasic, H. Zeng, A. R. Jones, C. Koch, E. S. Lein, Conserved cell types with divergent features in human versus mouse cortex. *Nature* **573**, 61–68 (2019).
63. W. Zhang, L. Ma, M. Yang, Q. Shao, J. Xu, Z. Lu, Z. Zhao, R. Chen, Y. Chai, J.-F. Chen, Cerebral organoid and mouse models reveal a RAB39b–PI3K–mTOR pathway-dependent dysregulation of cortical development leading to macrocephaly/autism phenotypes. *Gene Dev* **34**, 580–597 (2020).

Acknowledgments: We thank J.-F.C.'s laboratory colleagues for stimulating discussions. We are grateful for J. Sadan's critical reading of the manuscript. **Funding:** This work is supported by funds from the Associate Dean of Research Fund from the Center for Craniofacial Molecular Biology, Herman Ostrow School of Dentistry at the University of Southern California and grants R01DE030901 (to J.C.), R21AG075665 (to J.C.), and R21AG070681 (to J.C.) from the National Institutes of Health, USA. **Author contributions:** W.Z., M.Z., L.M., S.J., Q.C., and Z.Li. conceived and performed all experiments. Z. Lu helped with the manuscript writing. J.-F.C. and W.Z. designed and interpreted the experiments and wrote the manuscript. **Competing interests:** The authors declare that they have no competing interests. **Data and materials availability:** All data needed to evaluate the conclusions of the paper are present in the paper and/or the Supplementary Materials.

Submitted 2 August 2023
Accepted 3 January 2024
Published 2 February 2024
10.1126/sciadv.adk1034